applied sciences

MDPI

Article

Surrogate-Based Shape Optimization of a Cruciform Specimen for Biaxial Testing of Microparticle Reinforced Epoxy Adhesives

Burak Ergunes [1,2,*] and Mustafa Kemal Apalak [3]

[1] Unmanned Aerial Vehicle Technology and Operation Program, Department of Electronics and Automation, Technical Sciences Vocational School, Muş Alparslan University, Muş 49250, Türkiye
[2] Department of Mechanical Engineering, Graduate School of Natural and Applied Sciences, Erciyes University, Kayseri 38039, Türkiye
[3] Department of Mechanical Engineering, Erciyes University, Kayseri 38039, Türkiye; apalak@erciyes.edu.tr
* Correspondence: b.ergunes@alparslan.edu.tr

Abstract

Reliable determination of the in-plane biaxial mechanical behavior of particle-reinforced composite adhesives under multiaxial stress conditions requires cruciform specimen geometries that achieve high stress uniformity in the measurement zone. In this study, the elastic response obtained from uniaxial tensile tests was verified through representative volume element (RVE)-based micromechanical analyses by systematically examining mesh sensitivity and RVE edge size convergence across multiple random microparticle distributions under periodic boundary conditions. The probability density characterization of the effective elastic constants indicated that the remaining scatter is mainly governed by microstructural randomness and decreases as the RVE edge size increases, supporting a nearly direction-independent effective stiffness associated with the random microparticle distribution. The RVE-predicted mean tensile modulus remained in close agreement with experiments, with relative deviations of approximately −2% to +2% across the investigated reinforcement levels. The validated material parameters were based on a dynamic XGBoost (eXtreme Gradient Boosting) surrogate model driven by the geometric design variables, fillet radius and center thickness, combined with an adapted version of the LIPOTR (Lipschitz Optimization with Trust Region) algorithm. The initial and optimized geometries were then compared using both experimentally determined elastic properties and selected RVE-predicted engineering constants for the 2, 6, and 10 wt% materials. The significant reductions in the equivalent S_{eqv}, normal S_{11} and S_{22}, and shear S_{12} stress variations within the gauge zone of the optimized candidate geometry resulted in improved stress homogeneity.

Keywords: cruciform specimen; adhesive; particle reinforcement; representative volume element (RVE); shape optimization

Check for updates

Academic Editor: Camelia Cerbu

Received: 10 April 2026
Revised: 30 April 2026
Accepted: 8 May 2026
Published: 11 May 2026

Copyright: © 2026 by the authors. Licensee MDPI, Basel, Switzerland. This article is an open access article distributed under the terms and conditions of the Creative Commons Attribution (CC BY) license.

1. Introduction

Most materials are subjected to multiaxial loading under operating conditions. Structural adhesives are critical as joining elements, especially in performance-demanding industrial fields such as the aerospace, automotive, and defense industries. These adhesives are subjected to complex stress conditions such as shear, peel, and tensile stress under operating conditions [1]. In recent years, nano or microparticle reinforcements have been widely used to improve the mechanical properties of structural adhesives, such as toughness and strength. Because the particles in particle-reinforced composite adhesives are

randomly distributed and non-directional, they generally exhibit isotropic elastic behavior at the macroscale [2]. However, the mechanical properties of these materials are generally investigated using uniaxial tests. These methods do not adequately capture multiaxial stress states. Multiaxial testing methods are more precise for determining the multiaxial stress states [3].

Cruciform specimens are popular among researchers because the strain–stress response is more consistent across loading rates. To determine the planar biaxial mechanical properties of elastic materials such as metals, ceramics, composites, and biomaterials, this test specimen has been used for decades in planar biaxial tensile and compression tests. Despite their complex geometries and needs for accurate machining and manufacturing processes, they have important advantages in achieving a range of biaxial tensile stresses. They allow for evaluating damage theories under different loading conditions in tensile stress state [4–6]. The current composite testing standards for mechanical design data are largely uniaxial. Although various laboratories have proposed a standardized method for biaxial characterization, an established process is still necessary for polymer composites [7]. An optimized cruciform specimen adequate for the biaxial testing must meet the following requirements [8,9]: (1) maximum strain homogeneity in the central region of the biaxially loaded specimen, (2) minimized spherical shear deformations in the biaxially loaded test zone, (3) minimized strain concentrations or fracture formations outside the strain zone, (4) specimen fracture in the measurement zone at the specimen center, and (5) reproducible results. It is well known that it is challenging to develop a cruciform test specimen that fulfills all these requirements simultaneously. Therefore, researchers have carried out some numerical studies to optimize the shape of these specimens.

A finite element model (FEM) is an effective tool for optimizing cruciform specimens. The recent studies have shown that the geometric design of a cruciform specimen is effective; through shape optimization, stress homogeneity can be increased and boundary stress concentration can be reduced [10–12]. In this respect, the two most effective ways are either to reduce stress concentrations in the areas around the multiaxially loaded area, namely, the arms and corners, or to increase the stress by reducing the thickness in the measurement area. Before experimental verification, in general, the suitable geometry of the cruciform specimen was determined using FEM combined with parameter optimization methods [13]. Optimization problems in specimen geometry can be addressed by means of parametric or nonparametric approaches. In the parametric optimization approach, the most appropriate design of the cruciform specimen can be achieved by changing only the geometric parameters of the specimen elements, such as fillet and thickness, without altering the relations pertinent to the specimen design region. However, even if the parameter-optimization approach can improve the desired stress homogeneity and concentration in the cruciform specimen, a change in a single parameter fails to alter the nature of load transfer through the geometric features. Therefore, some researchers have focused on studies on the geometric design of cruciform specimens with parametric variations [8] and shape optimization [14].

One concern in the biaxial testing is to quantify the force (or stress) that is raised in the central region. Due to the geometric complexity of cruciform specimens, such as their thinner thickness relative to the intersection arms, higher stresses occur in the measurement region. Such a thickness variation is usually achieved by narrowing the path in the intersection arms. This can cause damage due to the stress homogeneity at the constriction surface in contact with the measurement area. Such a geometry of biaxial measuring region has been tried to obtain a homogeneous strain–stress situation, such as in the shapes of circles [15], rhombuses [16], and squares [17]. However, there is no agreement yet on the optimal shape of the unattached placement structure or on the biaxial

loading rate. Additionally, in cruciform specimens, the shapes of the corner radii formed by intersection arms can be changed by slits in the arms (as in metallic cruciform specimens). In this case, the stress analyses can be performed to direct the entire load applied to the arms of the cruciform specimen to the measurement area. As a result, the homogeneity of the stress and strain distributions in the measurement area can be further improved [18].

Mulay, A. and Bagul, V. [19] optimized the geometric parameters of the cruciform specimen in consideration of stress homogeneity and in-plane stress in the measurement region by using the Multi-Attribute Decision Making (MADM) methods and determined the optimal plate thickness, slot width, and corner radius values of the specimen. Yang, X. et al. [20] focused on optimizing the shape of a cruciform specimen using a genetic algorithm (GA) and a parametric modeling script (PMS). In the optimization process, a population was created, and the optimal geometric parameters were determined. These optimal parameters were used in a fitness function to increase the stress homogeneity in the center region and to reduce the stress concentration in the corner radii of the specimen. They reported that the stress distribution and deformation of the optimized specimen improved. Chen, J. et al. [14] used both topology and shape optimization algorithms to increase stress homogeneity in the measurement region of a cruciform specimen. The topology optimization was applied to distribute the biaxial load between the arms of the specimen. In contrast, the shape optimization was used to optimize the boundary shape at the crossroad of the cross-arms. Both optimization methods achieved the desired stress distribution and concentration improvements. Makris et al. [8] studied the mechanical behavior and shape optimization of carbon/epoxy cross-ply cruciform specimens under biaxial loading. They validated their finite element model using full-field strain measurements from Digital Image Correlation (DIC). Using a parametric optimization approach based on Sequential Quadratic Programming (SQP), they aimed to improve strain-field uniformity and reduce premature off-center damage in the gauge zone. The optimized Specimen A and Specimen B reduced the failure ratio (FR) by 57.8% and 71.2%. The coefficient of variation (CV) decreased by 9.2% and 17.8%, respectively, compared with a common reference geometry. Between the optimized designs, Specimen B showed the best overall performance.

In this study, the experimental data obtained from uniaxial tensile tests of a microparticle-reinforced epoxy composite adhesive was first validated using the representative volume element (RVE) micromechanical calculation method. The validated experimental data was then used to model material properties in the finite element analysis for an initial cruciform specimen geometry having parametric geometry variables, such as fillet radius (R) and center thickness (t). This cruciform specimen geometry with a parametric approach was created in a R-t space using Latin Hyper Sampling (LHS) for Design of Experiments (DOE). The initial geometries in this stage were then trained using the XGBoost (eXtreme Gradient Boosting) regression model, and then a dynamic window optimization framework adapted from Zhang's [21] was used to select the optimum geometry of the cruciform specimen. Following this optimization, the initial and optimized geometries were comparatively evaluated using finite element analyses with both experimentally determined elastic properties and engineering constants predicted by the selected RVE (for 2, 6, and 10 weight fractions). This study presented the determination of an optimized cruciform specimen geometry based on an experimentally defined reference material condition, together with the evaluation of its response under different reinforcement levels and material property definitions. The optimized shape of the cruciform specimen presented considerable improvements in the stress and strain homogeneity in the gauge zone in comparison to its initial state.

2. Materials and Methods

2.1. Specimen Preparation and Uniaxial Tensile Testing

In this study, the mechanical properties of the neat adhesive and composite adhesive specimens were determined; the experimental mechanical properties were used for the finite element models of these composite adhesive specimens with the RVE model. Finally, the successful RVE models were used for the stress analysis and shape optimization of the cruciform specimen. The composite adhesive specimens were prepared from neat epoxy and aluminum (Al) microparticles with a diameter of 75 μm at weight fractions of 2, 6, and 10%. These weight fractions were chosen to represent low, intermediate, and relatively high reinforcement levels within a practically castable range for composite adhesives. The selected weight fractions allow for evaluation of the effect of Al microparticle loading while limiting excessive increases in viscosity and casting difficulties associated with higher reinforcement content. A two-component structural adhesive (Kisling Ergo 7440; resin 7438 and hardener 7439; Kisling AG, Wetzikon, Switzerland) was selected as the polymer matrix. In addition, 75 μm-diameter aluminum microparticles were supplied by EgeNanotek (İzmir, Türkiye). The same production procedure was followed for the neat and the microparticle-reinforced epoxy adhesives during the preparation of ASTM D638-22 Type IV geometry [22].

Epoxy resin and hardener were weighed on a high-precision balance (KERN GmbH, Balingen, Germany) at a 1.96:1 (by weight) ratio, as recommended by the manufacturer. Neat epoxy adhesive specimens were poured directly into molds after degassing and mixing. For microparticle-reinforced specimens, Al microparticles were gradually added to the epoxy resin. To ensure a homogeneous distribution of microparticles, a manual premixing (10 min), a mechanical mixing (10 min), and an ultrasonic homogenization (Sxsonic, Shanghai, China) (15 min) were performed successively. The packets of cooling gels were wrapped around the beaker to prevent an increase in the temperature of the resin–particle mixture during the ultrasonic homogenization stage. In addition, this mixture was degassed in a vacuum oven (MIPROLAB, Ankara, Türkiye) for 5 min to remove air bubbles before and after the ultrasonic homogenization. Afterward, the hardener was added, and the mixture was remixed manually and mechanically, and then degassed in a vacuum oven for 10 min. The homogenized mixtures were poured into silicone molds and cured for 24 h at room temperature. The main stages of the specimen preparation process are schematically illustrated in Figure 1.

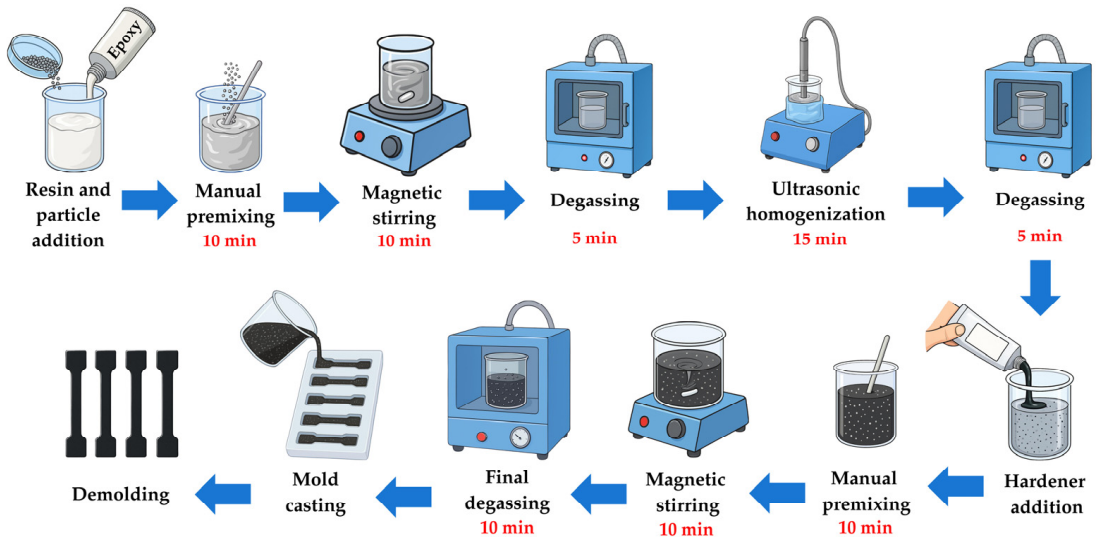


Figure 1. Schematic illustration of the specimen preparation process.

The uniaxial tensile tests were performed under standard laboratory conditions on a Shimadzu AGS-X 10 kN-capacity (Shimadzu Corporation, Kyoto, Japan) universal testing machine with a constant crosshead speed of 1 mm/min (Figure 2).

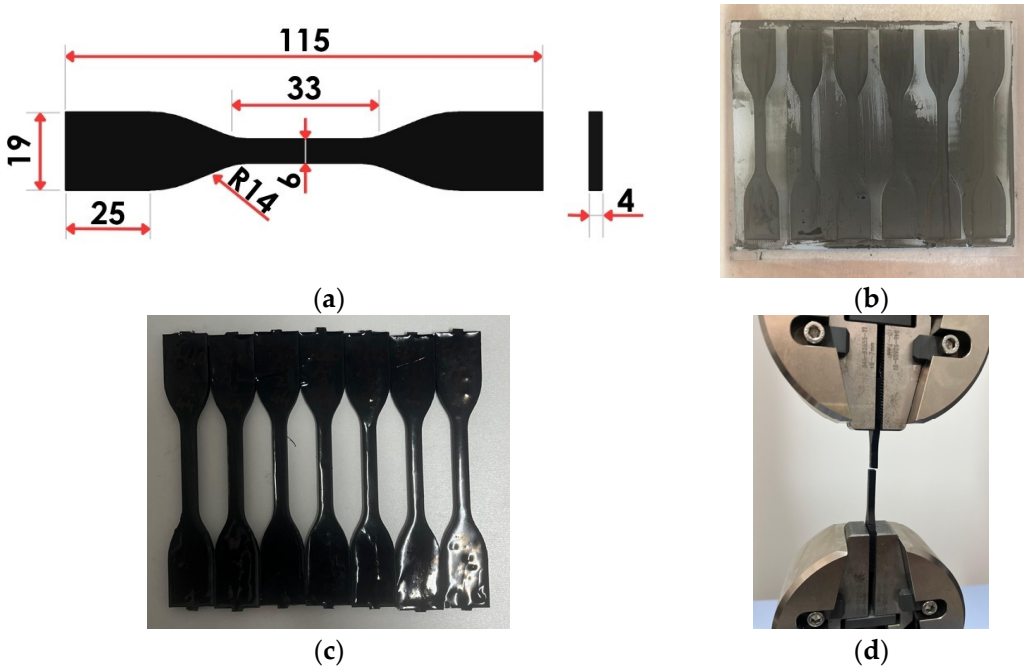


Figure 2. Specimen geometry, preparation, and test process: (**a**) specimen dimensions (in mm), (**b**) silicone mold casting, (**c**) produced specimens, and (**d**) tensile test.

The modulus of elasticity (E) was determined from the tensile tests using an ASTM approach procedure [22]. The engineering stress and diagrams were calculated from the measured data of force and elongation. To avoid bias from the initial toe region, a set of candidate strains was scanned within the early elastic regime (0.05–0.3%). The optimal strain windows, defined as the intervals providing the highest coefficient of determination (R^2) and the lowest root-mean-square error (RMSE) in the linear regression of the stress–strain curve, were selected to determine the linear elastic region of the curve. The mechanical properties of the neat epoxy adhesive, microparticle-reinforced composite adhesive specimens, and aluminum microparticles are given in Table 1, based on our experimental results and the manufacturer's data sheet.

Table 1. Properties of materials used in the RVE modeling.

Materials	Density (g/cm^3)	Tensile Modulus (GPa)	Poisson's Ratio
Aluminum microparticle	2.70 [1]	≈70 [1]	0.33 [1]
Neat epoxy adhesive	1.17 [2]	1.169 ± 0.037	0.33 [2]
2 wt% Al microparticle reinforced epoxy adhesive	-	1.181 ± 0.075	-
6 wt% Al microparticle reinforced epoxy adhesive	-	1.262 ± 0.047	-
10 wt% Al microparticle reinforced epoxy adhesive	-	1.269 ± 0.028	-

[1] According to the aluminum microparticle supplier's product information [23] and the literature values adopted for commercially pure aluminum powder elastic properties [24]. [2] According to the epoxy adhesive's manufacturer's data [25].

2.2. RVE Modeling and Mesh Convergence Study

2.2.1. RVE Model Setup

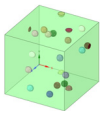
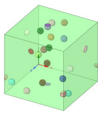
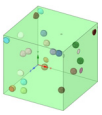
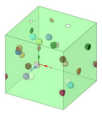
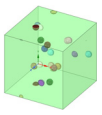
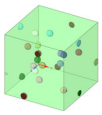
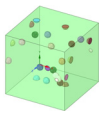
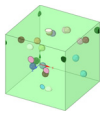
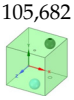
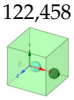
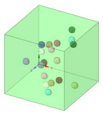
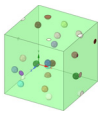
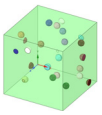
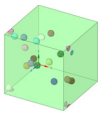
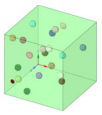
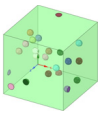
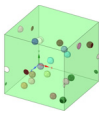
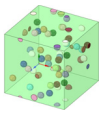
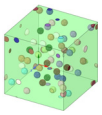
Representative volume element (RVE) models of aluminum microparticle-reinforced epoxy adhesives were generated in ANSYS Material Designer 2025 (ANSYS Inc., Canonsburg, PA, USA) using a finite element-based homogenization approach [26]. The material properties assigned to the matrix and reinforcement phases were taken from Table 1. As the RVE model is generated, the weight fraction of aluminum microparticles (wt.) was converted to a volume fraction, and the RVE model was developed for specific volume fraction of microparticles (Vf), namely, approximately 0.9, 2.7, and 4.6% for 2, 6, and 10 wt%, respectively. In the generated micro-structures, the epoxy phase was treated as the continuous matrix, whereas the reinforcement phase was represented by randomly distributed spherical aluminum microparticles. In ANSYS Material Designer, such random particle-reinforced systems are modeled as periodic unit cells composed of an isotropic linear–elastic matrix and spherical reinforcement phases with complete bonding at the matrix–particle interface.

Table 2 shows the random microparticle distributions in the RVEs having the smallest (300 μm) and largest (750 μm) edge sizes and the seed numbers arranging the random microparticle distributions for each weight fraction of microparticles. Each RVE has a statistically independent occurrence generated with a specific random seed; the seed numbers are listed above the RVE images and span fifteen different distributions (Seeds ID 1–15). Different seed numbers produce statistically independent RVE realizations for the same RVE edge size and microparticle weight fraction, which allows the influence of microstructural randomness on the effective material properties to be evaluated statistically. In ANSYS Material Designer, the seed numbers control the random generation of particle positions and, when applicable, particle diameters.

Cubic RVE models were created by enabling the ‘use conformal meshing’ and ‘use periodic meshing’ options in the mesh settings. ANSYS Material Designer automatically generates RVEs using SOLID187, a 10-node three-dimensional tetrahedral structural solid element that exhibits second-order displacement behavior. In the analysis settings, the anisotropy type was defined as orthotropic, and the ‘compute linear elasticity’ and ‘use periodic boundary conditions’ options were enabled. These analysis settings enabled the RVEs to be formulated as periodic unit cells within a finite element-based homogenization framework.

In ANSYS Material Designer, the orthotropic linear–elastic material properties are determined from six basic loading cases consisting of three normal loading conditions in the principal directions (X, Y, and Z) and three shear loading conditions in the orthogonal planes (XY, YZ, and XZ). In the periodic-boundary formulation, only one macroscopic strain component is prescribed for each loading case, while the remaining strain components are taken as zero. The resulting boundary reactions are then used to construct the homogenized stiffness matrix of the equivalent medium, from which the effective orthotropic engineering constants are calculated. In the present study, the moduli of elasticity (E_1, E_2, and E_3), shear moduli (G_{12}, G_{23}, and G_{13}), and Poisson’s ratios (ν_{12}, ν_{23}, and ν_{13}) were obtained for each RVE realization. Table 3 summarizes the number of particles used in the RVE models for different RVE edge sizes and microparticle weight fractions.

Table 2. Randomly generated RVE models.

wt%	RVE Edge Size (μm)	Random Microparticle Distributions							
Seed ID		1	2	3	4	5	6	7	8
Seed Numbers		36,683	53,749	65,271	20,667	12,172	1253	84,536	99,653
2	300								
	750								
	Seed ID	9	10	11	12	13	14		15
	Seed Numbers	105,682	122,458	980	2996	4903	564		8924
	300								
	750								
6		1	2	3	4	5	6	7	8
	Seed Numbers	36,683	53,749	65,271	20,667	12,172	1253	84,536	99,653
	300								
	750								
	Seed ID	9	10	11	12	13	14		15
	Seed Numbers	105,682	12,2458	980	2996	4903	564		8924
	300								
	750								
10		1	2	3	4	5	6	7	8
	Seed Numbers	36,683	53,749	65,271	20,667	12,172	1253	84,536	99,653
	300								
	750								
	Seed ID	9	10	11	12	13	14		15
	Seed Numbers	105,682	122,458	980	2996	4903	564		8924
	300								
	750								

Notes: The different particle colors are used only for visualization and do not indicate different material properties; all particles represent the same microparticle type.

Table 3. Number of particles used in the RVE models for different RVE edge sizes and microparticle weight fractions.

wt%	Number of Particles (Np) for Each RVE Edge Size (μm)					
	300	375	450	525	600	750
2	2	3	4	6	9	18
6	4	7	12	18	27	52
10	6	11	19	31	45	88

2.2.2. Mesh Convergence

In order to minimize the dependency of the finite element analyses on the mesh size and to ensure that the RVE model could produce stable elastic constants, a mesh convergence study was first performed. An RVE model in the dimensions of 375 × 375 × 375 μm was created using ANSYS Material Designer, and it was evaluated for 15 different random seed numbers and the finite element sizes ranging from 18 to 4 μm. The predicted modulus of elasticity E_1, E_2, and E_3 values, the required total number of elements, and CPU elapsed times were noted from the finite element analyses and are presented in Table 4.

Table 4. Effect of the finite element size and microparticle weight fraction on the predicted directional elastic moduli, total number of nodes and elements, and elapsed time.

wt%	Finite Element Size (μm)	Directional Elastic Moduli (MPa)			Total Number of		Elapsed Time (min)
		E_1	E_2	E_3	Nodes	Elements	
2	18	1198.633 ± 0.39	1198.713 ± 0.79	1198.707 ± 0.65	129,745	91,028	<3
	16	1198.580 ± 0.40	1198.687 ± 0.79	1198.693 ± 0.66	174,888	123,319	<4
	14	1198.567 ± 0.40	1198.653 ± 0.78	1198.627 ± 0.64	257,108	182,331	<5
	12	1198.540 ± 0.39	1198.620 ± 0.77	1198.613 ± 0.65	402,757	287,908	<6
	10	1198.507 ± 0.39	1198.607 ± 0.78	1198.607 ± 0.65	682,737	492,245	<10
	8	1198.493 ± 0.38	1198.587 ± 0.79	1198.600 ± 0.65	1,324,714	961,135	<20
	6	1198.413 ± 0.34	1198.567 ± 0.77	1198.587 ± 0.66	3,055,375	2,232,376	<35
	4	1198.480 ± 0.39	1198.580 ± 0.77	1198.580 ± 0.65	9,964,187	7,339,058	<140
6	18	1240.213 ± 1.69	1240.553 ± 2.38	1241.093 ± 2.64	131,612	92,275	<3
	16	1240.140 ± 1.69	1240.453 ± 2.37	1240.993 ± 2.64	177,406	125,042	<4
	14	1240.053 ± 1.68	1240.373 ± 2.37	1240.913 ± 2.64	260,383	184,538	<4
	12	1239.973 ± 1.68	1240.320 ± 2.36	1240.860 ± 2.63	405,431	289,809	<6
	10	1239.940 ± 1.69	1240.253 ± 2.33	1240.793 ± 2.61	685,053	493,998	<10
	8	1239.900 ± 1.69	1240.233 ± 2.34	1240.773 ± 2.62	1,327,456	963,182	<20
	6	1239.867 ± 1.67	1240.220 ± 2.34	1240.760 ± 2.63	3,052,833	2,230,809	<35
	4	1239.867 ± 1.67	1240.207 ± 2.34	1240.747 ± 2.61	9,964,075	7,339,720	<150
10	18	1284.673 ± 3.63	1284.880 ± 3.63	1284.213 ± 2.90	134,089	93,919	<3
	16	1284.547 ± 3.64	1284.753 ± 3.60	1284.073 ± 2.88	180,981	127,451	<4
	14	1284.400 ± 3.64	1284.580 ± 3.58	1283.947 ± 2.90	264,030	186,952	<5
	12	1284.280 ± 3.61	1284.480 ± 3.58	1283.833 ± 2.88	408,593	291,947	<6
	10	1284.180 ± 3.60	1284.393 ± 3.57	1283.747 ± 2.87	686,376	494,935	<10
	8	1284.153 ± 3.60	1284.340 ± 3.56	1283.693 ± 2.85	1,329,508	964,719	<25
	6	1284.107 ± 3.58	1284.307 ± 3.55	1283.660 ± 2.86	3,051,871	2,230,463	<40
	4	1284.100 ± 3.58	1284.287 ± 3.56	1283.647 ± 2.87	9,971,431	7,346,163	<160

Figure 3a–c show the effect of finite element size on the predicted directional elastic moduli (E_1–E_3), and the elapsed time for the RVEs having the microparticle distributions at the weight fractions of 2, 6, and 10%. For all weight fractions of microparticles, the moduli of elasticity converge to specific values with mesh refinement, namely, as the finite element size approaches a level of 8–10 μ. However, this results in a significantly increasing computational cost. To quantify the effects, three systematically refined mesh

levels of 16, 8, and 4 μm with a constant refinement ratio of r = 2 were considered, where $r = \frac{h_{coarse}}{h_{fine}}$ indicates that the characteristic element size was reduced by one half at each refinement step. Richardson extrapolation [27] was employed to estimate the asymptotic, mesh-independent response, while the Grid Convergence Index (GCI) [28,29] was used to quantify the remaining mesh-induced numerical uncertainty of the selected discretization. The numerical response can be expressed in the asymptotic form $\varnothing\,(h) = \varnothing_{ext} + ah^p$, where $\varnothing_{ext}$ denotes the extrapolated mesh-independent value, while the GCI provides a normalized measure of the discretization uncertainty based on systematically refined meshes. Accordingly, the horizontal asymptote lines in Figure 3 represent the Richardson-extrapolated values, whereas the error bars at 8 μm indicate the GCI-based uncertainty of the adopted mesh. The uncertainty at 8 μm was lower across all cases, ranging from 0.000745% to 0.006006%, corresponding to 0.008929–0.077124 MPa in the predicted moduli of elasticity. In contrast, as the mesh size is reduced from 8 μm to 4 μm, the elapsed calculation time is increased by 7.7–8.5 times, and a negligible improvement is achieved in the predicted E_1, E_2, and E_3 values. Therefore, by taking into account both accuracy and computational cost, the more suitable finite element mesh size was set to 8 μm for all weight fractions and was implemented for all subsequent RVE analyses.

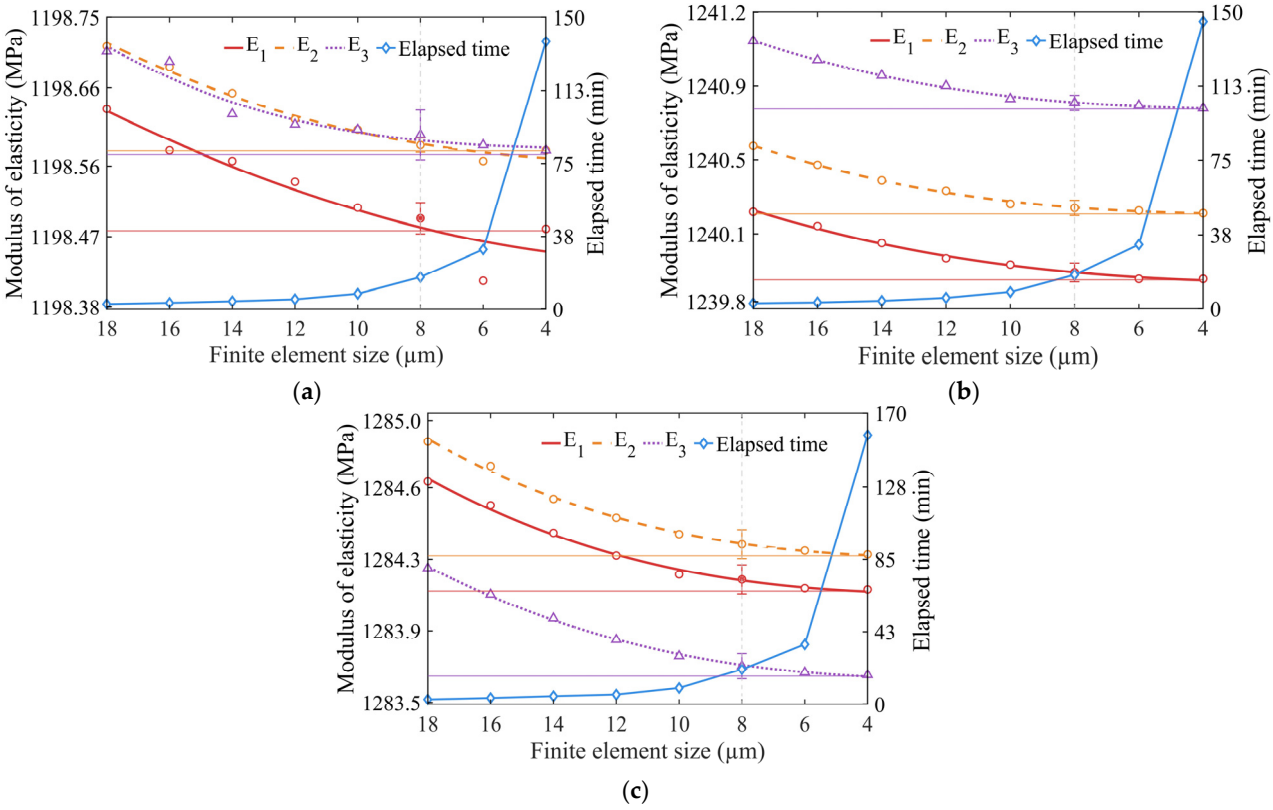


Figure 3. The variations in the moduli of elasticity (E_1, E_2 and E_3) and the elapsed time with the finite element size for various weight fractions of microparticles, (**a**) 2 wt%, (**b**) 6 wt% and (**c**) 10 wt%.

2.3. RVE Edge Size Convergence and Selection of Homogenized Engineering Constants

2.3.1. Statistical Convergence of the RVE-Predicted Engineering Constants

The statistical convergence of RVE-based homogenization results was evaluated by examining the distributions of centered errors for the predicted elastic and shear moduli. Table 5 shows the probability density (φ) variations in the errors in the predicted modulus of elasticity (E_i) and in the predicted shear modulus (G_{ij}) for various RVE edge sizes and weight fractions of microparticles. For each weight fraction (2, 6 and 10%), six different RVE edge sizes (300, 375, 450, 525, 600 and 750 μm) were considered, and the random

microparticle distributions were generated using 15 independent random seed numbers. The finite element analysis for each RVE configuration was performed and three moduli of elasticity E_i and shear moduli G_{ij} were calculated. For the moduli of elasticity E_i, the errors vary in ranges of [−2.5, 2.5], [−10, 10], and [−15, 15] MPa for weight fractions of 2, 6 and 10%, respectively. The probability density has upper limits of 3.1723, 0.69256, and 0.4117, respectively. The error levels increase partly with increasing weight fractions, but are very small for all weight fractions and microparticle sizes in comparison to the predicted modulus values (1190–1290 MPa). In addition, the errors in the predicted shear moduli G_{ij} vary in ranges of [−2.5, 2.5], [−5, 5], and [−5, 5] MPa for weight fractions of 2, 6 and 10%, respectively. The corresponding probability density has upper limits of 6.9538, 2.9115, and 1.4514, respectively. The error levels increase slightly with increasing weight fractions, but are negligible for all weight fractions and microparticle sizes in comparison to the predicted shear modulus values (447–486 MPa).

Table 5. Probability density variations in the errors in the predicted moduli of elasticity (E_i) and shear moduli (G_{ij}) for various RVE edge sizes and weight fractions.

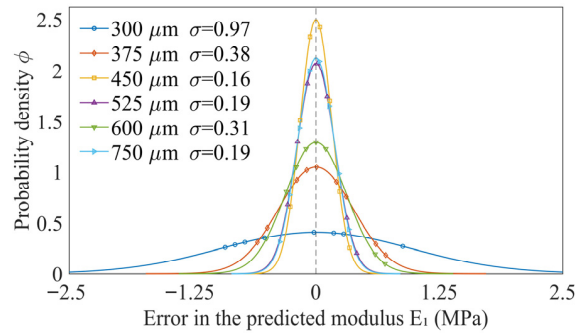
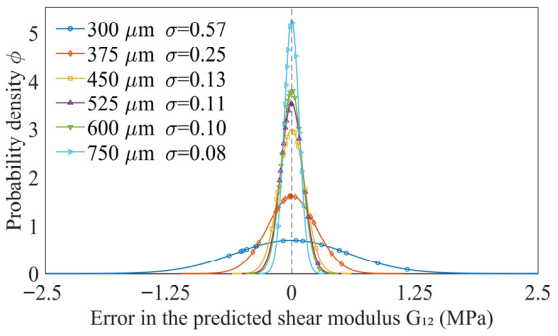
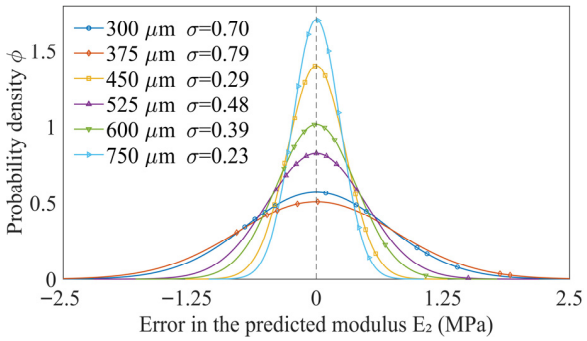
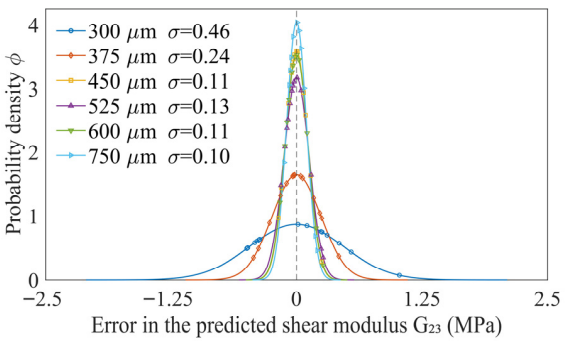
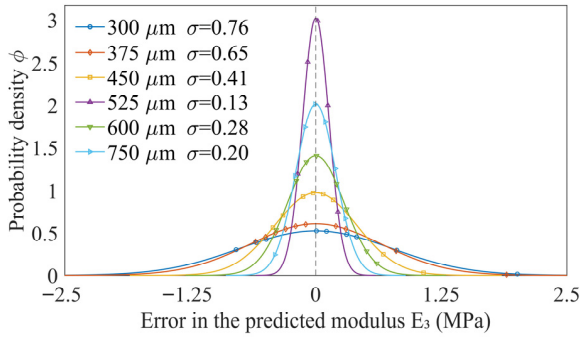
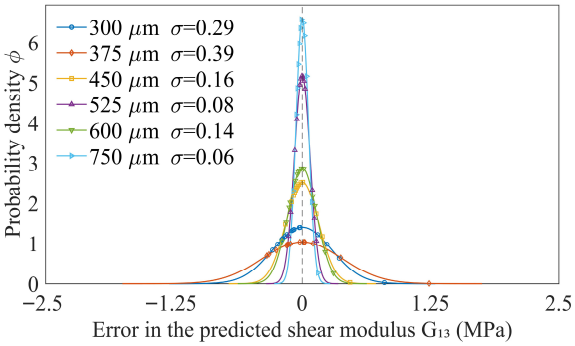
wt%	Modulus of Elasticity, E_i	Shear Modulus, G_{ij}
2		
		
		

Table 5. *Cont.*

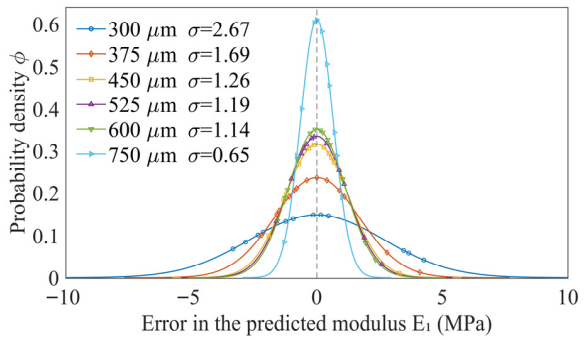
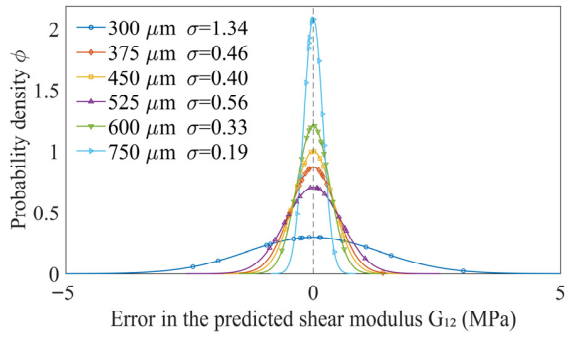
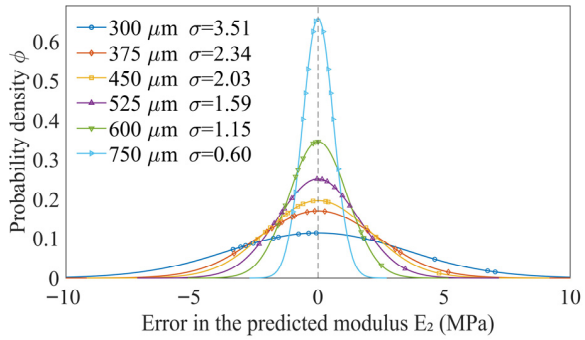
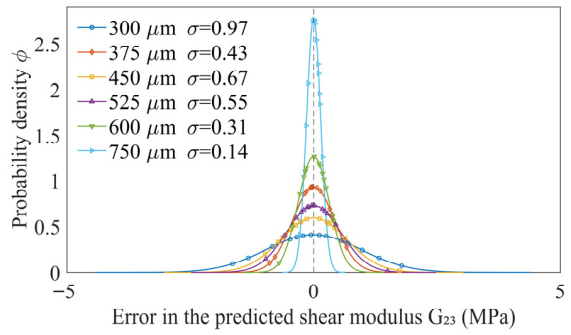
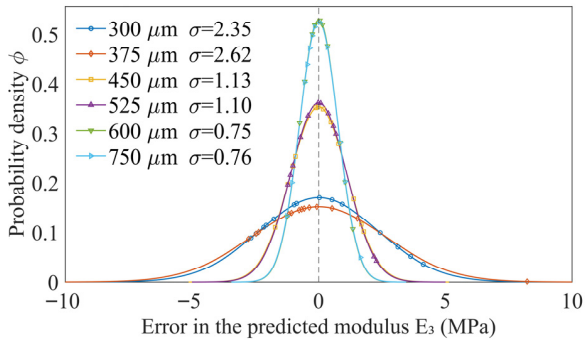
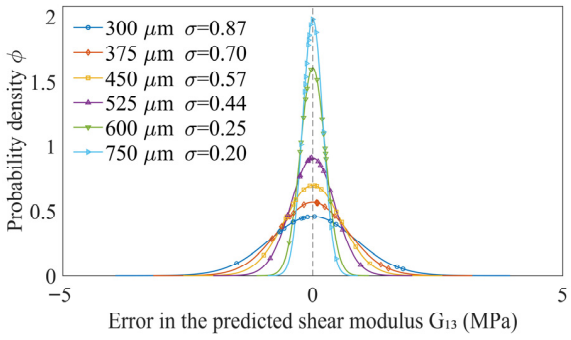
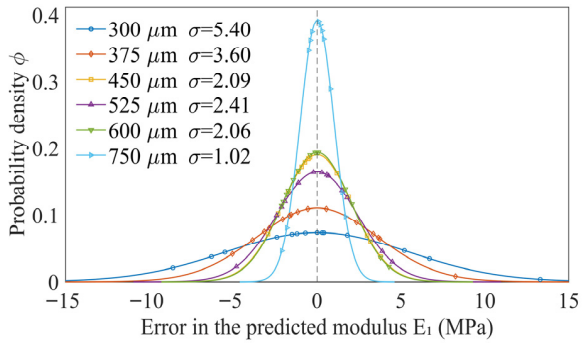
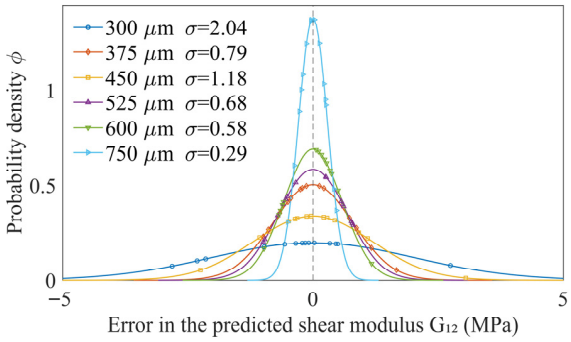
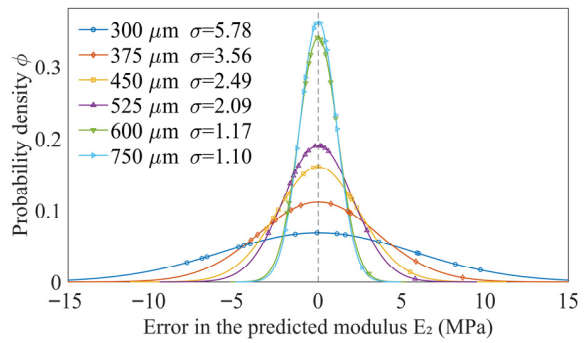
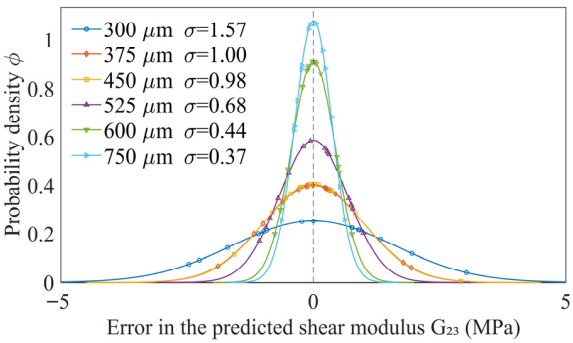
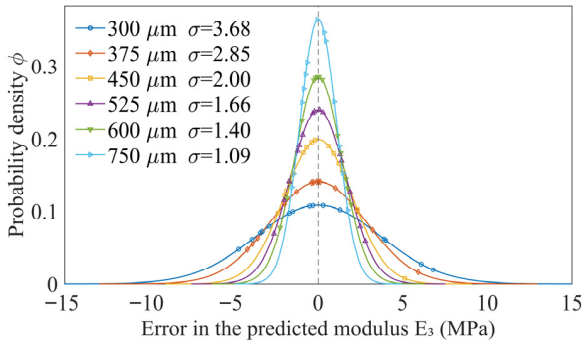
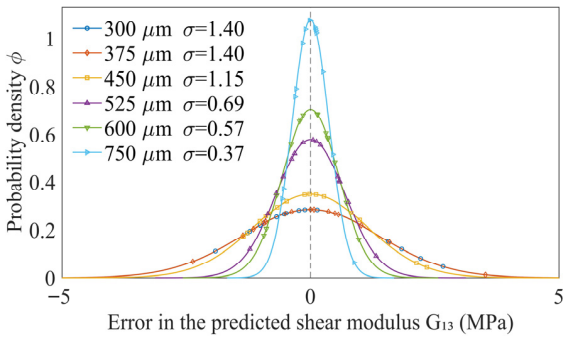
wt%	Modulus of Elasticity, E_i	Shear Modulus, G_{ij}
6		
		
		
10		
		

Table 5. *Cont.*

wt%	Modulus of Elasticity, E_i	Shear Modulus, G_{ij}
10		

In case the probability density variations are compared (Table 5), for all weight fractions, the errors in the distributions of modulus of elasticity and shear modulus become more compact as the RVE edge size increases. The common errors for 15 different random microparticle distribution seed numbers are spread over a wider range at small RVE edge sizes (300 and 375 μm) and are clustered in a significantly narrower band within the same error windows at large RVE edge sizes (600 and 750 μm). For example, typical standard deviation levels in E_i decreased from approximately ± (0.7–1.0) MPa at 2 wt%, ± (2.4–3.5) MPa at 6 wt%, and ± (3.7–5.8) MPa at 10 wt% to significantly lower levels at RVE edge sizes of 600 and 750 μm. This trend is similarly observed in those of G_{ij}. Although some graphs show transient broadening or different contraction rates in the RVE edge size range of 375–525 μm, a larger RVE edge size represents the regions where seed-induced deviations are most consistently observed for all constants. These typical changes indicate a transition from sensitive responses at small RVE edge sizes to a statistically more stable regime at larger RVE edge sizes. In case the E_i and G_{ij} groups are evaluated together within the same weight fractions, the distribution of error variations according to RVE edge sizes continues. Although a non-monotonic behavior is observed in E_i components at some intermediate RVE edge sizes (375–525 μm)—for example, a significant probability density reduction in E_1 around 450 μm at 2 wt%, and a more gradual recovery in E_2—these differences decrease significantly at the RVE edge sizes of 600 and 750 μm.

2.3.2. Experimental Validation of the Predicted Elastic Moduli

Table 6 summarizes the effect of RVE edge size on the predicted mean elastic modulus (E_{mean}) and the corresponding error relative to the experimental modulus (E_{exp}) for aluminum microparticle-reinforced epoxy adhesives at 2, 6, and 10 wt%. For each weight fraction, the predicted mean modulus values obtained from RVE edge sizes between 300 and 750 μm are reported together with the percentage error according to the experimentally measured modulus of elasticity. The comparison between E_{mean} and E_{exp} shows that the predicted elastic modulus approaches a stable range as the RVE edge size increases for all weight fractions. At 2 wt%, the error decreases from +2.30% at 300 μm to +0.86% at 750 μm, while the predicted modulus becomes nearly stable after 450 μm. At 6 wt%, the error remains within the range of −1.03% to −2.14%, indicating a slight underestimation of the experimental modulus, whereas at 10 wt%, the error stays within a narrow interval between +1.14% and +1.85%, showing a close agreement with the experimental results throughout the entire RVE size range. The comparison presented in Table 6 indicates that the proposed homogenization-based micromechanical model can predict the experimental modulus of elasticity with a low error level for all weight fractions and provides a reliable representation of the effective elastic response.

Table 6. Effect of RVE edge size on the predicted mean elastic modulus and the corresponding error relative to the experimental modulus for different weight ratios of aluminum microparticles.

wt%	RVE Edge Size (μm)	E_{mean} (MPa)	Error in E_{exp} (%)
2	300	1208.01 ± 0.47	+2.30
	375	1198.56 ± 0.36	+1.50
	450	1191.63 ± 0.18	+0.92
	525	1190.35 ± 0.18	+0.81
	600	1190.47 ± 0.19	+0.82
	750	1190.99 ± 0.12	+0.86
6	300	1248.86 ± 1.67	−1.03
	375	1240.30 ± 1.30	−1.70
	450	1239.68 ± 0.88	−1.75
	525	1235.69 ± 0.76	−2.07
	600	1235.74 ± 0.59	−2.07
	750	1234.82 ± 0.39	−2.14
10	300	1292.46 ± 2.91	+1.85
	375	1284.06 ± 1.94	+1.19
	450	1283.80 ± 1.27	+1.17
	525	1287.08 ± 1.20	+1.42
	600	1283.98 ± 0.92	+1.18
	750	1283.44 ± 0.62	+1.14

2.3.3. Selection of Homogenized Engineering Constants for FEA

Table 7 summarizes the predicted homogenized engineering constants obtained for 2, 6, and 10% weight fractions of microparticle-reinforced epoxy adhesives at different RVE edge sizes. The values given in the table represent the mean and standard deviation calculated from 15 different random distributions at the respective RVE edge sizes. Therefore, the variation in engineering constants E_1, E_2, E_3, G_{12}, G_{23}, G_{13}, ν_{12}, ν_{23}, and ν_{13} with regard to RVE size and the level of dispersion between the distributions of these engineering constants can be evaluated together. The determination of the homogenized engineering constants to be used in FEA was not based only on the direct selection of results belonging to the largest RVE size. Rather, the selection procedure was treated as a systematic decision-making process that considers both the convergence behavior of apparent engineering constants with regard to RVE size and the statistical stability of these results.

The selection procedure was established based on the set of stiffness-related engineering constants $S = \{E_1, E_2, E_3, G_{12}, G_{23}, G_{13}\}$. Although Poisson's ratios were monitored throughout the analysis, they were not included in the primary decision criterion. For each candidate RVE edge size L, the mean value $\mu_\phi(L)$ and the standard deviation $s_\phi(L)$ of each engineering constant were calculated from the 15 random distributions. The selection was then defined in terms of three complementary statistical indicators.

Table 7. Predicted homogenized engineering constants at different RVE edge sizes.

wt%	RVE Edge Size (μm)	E_1 (MPa)	E_2 (MPa)	E_3 (MPa)	G_{12} (MPa)	G_{23} (MPa)	G_{13} (MPa)	ν_{12} (-)	ν_{23} (-)	ν_{13} (-)
2	300	1208.12 ± 0.97	1207.91 ± 0.70	1207.99 ± 0.76	454.48 ± 0.57	454.42 ± 0.46	454.14 ± 0.29	0.3286 ± 0.0005	0.3286 ± 0.0004	0.3283 ± 0.0004
	375	1198.49 ± 0.38	1198.58 ± 0.79	1198.60 ± 0.65	450.90 ± 0.25	450.97 ± 0.24	450.87 ± 0.39	0.3289 ± 0.0003	0.3289 ± 0.0004	0.3288 ± 0.0002
	450	1191.56 ± 0.16	1191.61 ± 0.29	1191.73 ± 0.41	448.21 ± 0.13	448.26 ± 0.11	448.24 ± 0.16	0.3291 ± 0.0001	0.3291 ± 0.0001	0.3291 ± 0.0002
	525	1190.26 ± 0.19	1190.40 ± 0.48	1190.38 ± 0.13	447.76 ± 0.11	447.82 ± 0.13	447.71 ± 0.08	0.3292 ± 0.0002	0.3292 ± 0.0001	0.3292 ± 0.0001
	600	1190.50 ± 0.31	1190.42 ± 0.39	1190.49 ± 0.28	447.80 ± 0.10	447.85 ± 0.11	447.81 ± 0.14	0.3292 ± 0.0001	0.3292 ± 0.0001	0.3292 ± 0.0001
	750	1190.97 ± 0.19	1190.98 ± 0.23	1191.01 ± 0.20	448.03 ± 0.08	448.05 ± 0.10	448.02 ± 0.06	0.3292 ± 0.0001	0.3292 ± 0.0001	0.3292 ± 0.0001
6	300	1249.14 ± 2.67	1248.87 ± 3.51	1248.57 ± 2.35	470.28 ± 1.34	470.37 ± 0.97	469.92 ± 0.87	0.3270 ± 0.0014	0.3272 ± 0.0012	0.3269 ± 0.0009
	375	1239.90 ± 1.69	1240.23 ± 2.34	1240.77 ± 2.62	466.73 ± 0.46	467.04 ± 0.43	466.72 ± 0.70	0.3273 ± 0.0009	0.3272 ± 0.0009	0.3271 ± 0.0010
	450	1239.52 ± 1.26	1240.00 ± 2.03	1239.52 ± 1.13	466.60 ± 0.40	466.93 ± 0.67	466.77 ± 0.57	0.3271 ± 0.0006	0.3274 ± 0.0005	0.3275 ± 0.0005
	525	1235.51 ± 1.19	1235.94 ± 1.59	1235.62 ± 1.10	465.21 ± 0.56	465.40 ± 0.55	465.19 ± 0.44	0.3274 ± 0.0005	0.3275 ± 0.0005	0.3275 ± 0.0004
	600	1235.87 ± 1.14	1235.79 ± 1.15	1235.55 ± 0.75	465.36 ± 0.33	465.58 ± 0.31	465.30 ± 0.25	0.3274 ± 0.0004	0.3277 ± 0.0003	0.3275 ± 0.0003
	750	1234.80 ± 0.65	1234.70 ± 0.60	1234.95 ± 0.76	464.93 ± 0.19	465.02 ± 0.14	465.05 ± 0.20	0.3275 ± 0.0002	0.3275 ± 0.0003	0.3275 ± 0.0002
10	300	1292.80 ± 5.40	1292.27 ± 5.78	1292.31 ± 3.68	486.88 ± 2.04	486.99 ± 1.57	486.29 ± 1.40	0.3255 ± 0.0021	0.3256 ± 0.0017	0.3251 ± 0.0017
	375	1284.15 ± 3.60	1284.34 ± 3.56	1283.69 ± 2.85	483.64 ± 0.79	483.65 ± 1.00	483.50 ± 1.40	0.3256 ± 0.0009	0.3258 ± 0.0009	0.3258 ± 0.0012
	450	1284.33 ± 2.09	1283.99 ± 2.49	1283.09 ± 2.00	484.18 ± 1.18	484.01 ± 0.98	483.58 ± 1.15	0.3257 ± 0.0006	0.3261 ± 0.0009	0.3258 ± 0.0007
	525	1287.02 ± 2.41	1287.29 ± 2.09	1286.92 ± 1.66	485.25 ± 0.68	485.44 ± 0.68	485.01 ± 0.69	0.3256 ± 0.0006	0.3258 ± 0.0008	0.3256 ± 0.0006
	600	1284.02 ± 2.06	1283.65 ± 1.17	1284.26 ± 1.40	483.78 ± 0.58	483.88 ± 0.44	483.81 ± 0.57	0.3258 ± 0.0004	0.3257 ± 0.0006	0.3256 ± 0.0005
	750	1283.51 ± 1.02	1283.37 ± 1.10	1283.45 ± 1.09	483.84 ± 0.29	484.06 ± 0.37	484.06 ± 0.37	0.3257 ± 0.0003	0.3258 ± 0.0003	0.3258 ± 0.0003

The first indicator was the relative mean deviation, introduced to quantify how closely the mean value obtained at a candidate RVE size approached the solution regarded as stabilized at a larger RVE size. For this aim, the largest analyzed RVE size ($L_{ref} = 750$ μm) was taken as a practical numerical reference, and the following expression was used for each $\phi \in S$:

$$\delta_\phi(L) = \frac{|\mu_\phi(L) - \mu_\phi(L_{ref})|}{|\mu_\phi(L_{ref})|} \times 100$$

This quantity represents the relative difference between the mean apparent constant obtained at a given candidate RVE size and the corresponding reference solution. The second indicator was the coefficient of variation, which represents the relative scatter among distributions at the same RVE size:

$$CV_\phi(L) = \frac{s_\phi(L)}{|\mu_\phi(L)|} \times 100$$

Since this expression gives the ratio of the standard deviation to the mean value, it enables the scatter level of engineering constants with different magnitudes to be compared on a common basis. The third indicator was the normalized half-width of the two-sided 95% confidence interval, introduced to assess the statistical reliability of the estimated mean:

$$CI_\phi(L) = \frac{t_{0.975,14}\, s_\phi(L)}{\sqrt{15}|\mu_\phi(L)|} \times 100$$

where $t_{0.975,14}$ denotes the critical value of Student's t-distribution corresponding to a two-sided 95% confidence interval with 14 degrees of freedom. This indicator represents the statistical reliability of the estimated mean. Accordingly, $\delta_\phi(L)$, $CV_\phi(L)$, and $CI_\phi(L)$ were employed as three complementary indicators describing, respectively, the convergence of the mean value toward the reference solution, the realization-to-realization scatter, and the uncertainty associated with the estimated mean. To ensure a conservative selection, the decision was not made separately for each engineering constant. Instead, the worst-case value was retained for each metric:

$$\delta_{max}(L) = \max_{\phi \in S} \delta_\phi(L), \quad CV_{max}(L) = \max_{\phi \in S} CV_\phi(L), \quad CI_{max}(L) = \max_{\phi \in S} CI_\phi(L)$$

These worst-case indicators were then normalized by prescribed acceptance thresholds,

$$\eta_\delta(L) = \frac{\delta_{max}(L)}{\delta_{allow}}, \quad \eta_{CV}(L) = \frac{CV_{max}(L)}{CV_{allow}}, \quad \eta_{CI}(L) = \frac{CI_{max}(L)}{CI_{allow}}$$

with $\delta_{allow} = 0.10\%$, $CV = 0.15\%$, and $CI_{allow} = 0.10\%$. These thresholds are defined as selection tolerances that simultaneously represent sufficient average stability, limited scattering between random distributions, and acceptable confidence interval width for the homogenized engineering constants to be selected. In this way, three statistical quantities with different physical meanings are made dimensionless and combined under a common decision criterion. Rather than serving as a rigid automatic pass/fail criterion, the normalized indicators were considered together to evaluate the evolution of convergence and statistical stability with increasing RVE size. On the basis, the final selection was made by jointly interpreting $\eta_\delta(L)$, $\eta_{CV}(L)$, and $\eta_{CI}(L)$, with the aim of identifying the practically suitable RVE size that provided a sufficiently stabilized mean response, limited realization-to-realization scatter, and adequate statistical reliability for subsequent FEA. In this context, the prescribed thresholds were treated as selection tolerances guiding the

assessment, rather than as strict cut-off values. The corresponding threshold-normalized worst-case convergence indicators are presented in Figure 4.

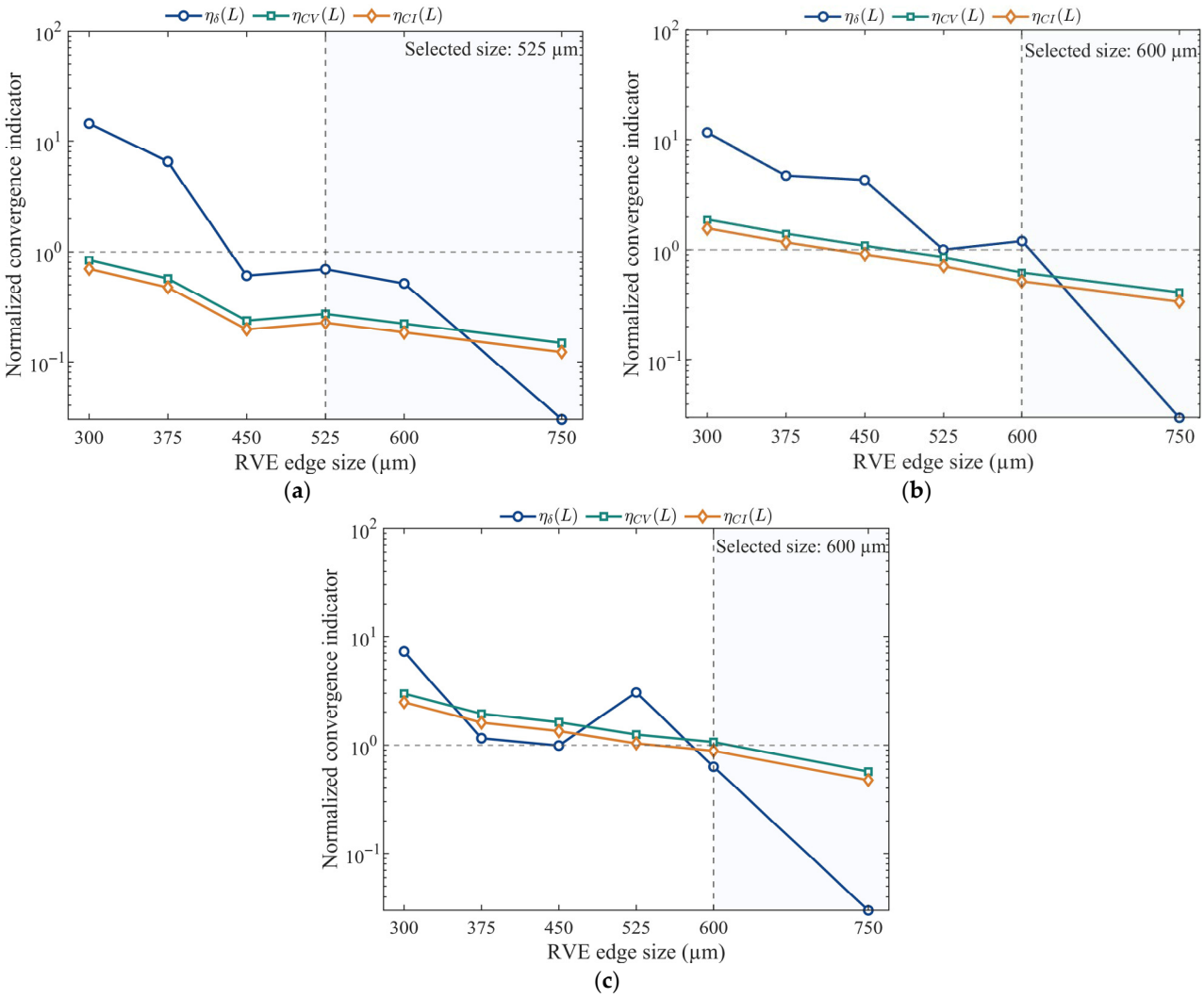


Figure 4. Selection of RVE edge size for the predicted homogenized engineering constants of microparticle-reinforced epoxy adhesives at (**a**) 2 wt%, (**b**) 6 wt%, and (**c**) 10 wt%.

According to Figure 4, the effect of RVE edge size on the convergence and statistical stability of the predicted homogenized engineering constants differs among the three materials, and this difference directly governed the final selection. For the 2 wt% material, the most pronounced improvement occurred between 300 and 450 μm, where $\eta_\delta(L)$ decreases from 14.40 to 0.6045, while $\eta_{CV}(L)$ and $\eta_{CI}(L)$ decrease from 0.8391 and 0.6970 to 0.2350 and 0.1952, respectively; beyond this range, all three indicators remain at low levels, indicating that the apparent engineering constants have already entered a stable plateau regime, and 525 μm was therefore adopted as a conservative yet still efficient choice within this stabilized region. For the 6 wt% material, the transition to a stable regime is more gradual; nevertheless, the change from 525 to 600 μm still yields a meaningful reduction in $\eta_{CV}(L)$ and $\eta_{CI}(L)$, from 0.8576 and 0.7124 to 0.6220 and 0.5167, respectively, indicating improved statistical robustness, and 600 μm was therefore considered the most suitable practical choice. A similar but more pronounced trend is observed for the 10 wt% material, for which the change from 525 to 600 μm leads to a substantial improvement in all three indicators, with $\eta_\delta(L)$ decreasing from 3.0545 to 0.6311, $\eta_{CV}(L)$ from 1.2499 to 1.0690, and $\eta_{CI}(L)$ from 1.0383 to 0.8880; thus, 600 μm represents the first RVE size at which the mean

response becomes clearly stabilized and the statistical reliability becomes acceptable, while the additional improvement obtained at 750 μm is comparatively limited. On this basis, 525 μm for the 2 wt% and 600 μm for the 6 and 10 wt% materials were identified as the most suitable practical RVE sizes for the subsequent FEA.

3. Shape Optimization Processes (Cruciform Specimen)

This study combines a dynamically adaptive surrogate-assisted search strategy with implicit finite element analysis (FEA) for the shape optimization in order to determine an optimal cruciform geometry that can improve stress homogeneity under a biaxial loading. A parametric model of cruciform geometry was created using the fillet radius and center thickness as the main shape parameters, with a dual-objective formulation that aims to improve homogeneity within the selected gauge zone. The optimization proceeds through an iterative loop in which the FEA-calculated results are used to train an XGBoost surrogate model, and the design space is successively refined by a dynamic window-shrinkage mechanism that concentrates sampling in the most promising region of R-t design vector space.

3.1. Finite Element Model (FEM) Setup

A cruciform specimen with a thinned center was created using FEM in order to characterize nominal stress accurately. To improve stress uniformity in the measurement region and to reduce stress concentration in the cross-arms, the specimen geometry was parametrically adjusted for the thickness (t) of the thinned center region and the radius (R) of the rounded corners. These two geometric variables were chosen because they directly alter the stress distribution in the central measurement region while maintaining the specimen's external dimensions, grip conformity, and ease of silicone mold fabrication. The remaining geometric features, including arm width, tapered profile, slot configuration, and measurement region shape, were kept constant to ensure consistent specimen design, boundary condition definition, and mold configuration throughout the numerical comparison. The initial cruciform specimen geometry with a thinned center gauge zone was created according to our in-plane biaxial testing system (Figure 5). The specimen dimensions include a clamping part, specimen geometry, and the center-reduced area of the specimen. The clamping part length, width and thickness are taken as 25, 25 and 4 mm, respectively. The cross-shaped specimen has a total length of 120 mm, a total width of 120 mm, rounded corners of 6 mm, a thickness of 4 mm, and cross-arm lengths of 60 mm. The edge length and thickness of the thinned center region are 20 mm and 2 mm, respectively.

To reduce computational costs without compromising accuracy, only one-quarter finite element model of the cruciform specimen was considered, leveraging geometric and loading symmetry (Figure 6a). To enforce symmetry constraints, the symmetric boundary conditions (x = 0, y = 0) were applied to the planes, namely, the displacements perpendicular to each plane were suppressed, thereby stabilizing out-of-plane motion and preventing rigid-body rotation. A quadratic tetrahedral element, SOLID187, was used for the mesh of the specimen. Element size was set to 0.1 mm for the fillet and gauge zones, and 0.5 mm for the arms and other regions. A Jacobian ratio in a validity range of 1 to 1.163 was used to assess mesh quality. The generated quarter model contained approximately 1.37 million nodes and 0.94 million elements. To ensure consistent comparison of objective function values, the same mesh generation process—which includes element size distribution, local mesh refinement strategy, and mesh quality criteria—was applied to all candidate geometries. Biaxial loading was applied to the clamp zone ends via rigid remote displacement boundary conditions to ensure a smooth motion (Figure 6b). A symmetric biaxial loading condition was created by applying a displacement of −0.25 mm in the Y-direction from the

positive Y arm. In comparison, the positive X arm was constrained with a displacement of +0.25 mm in the X-direction.

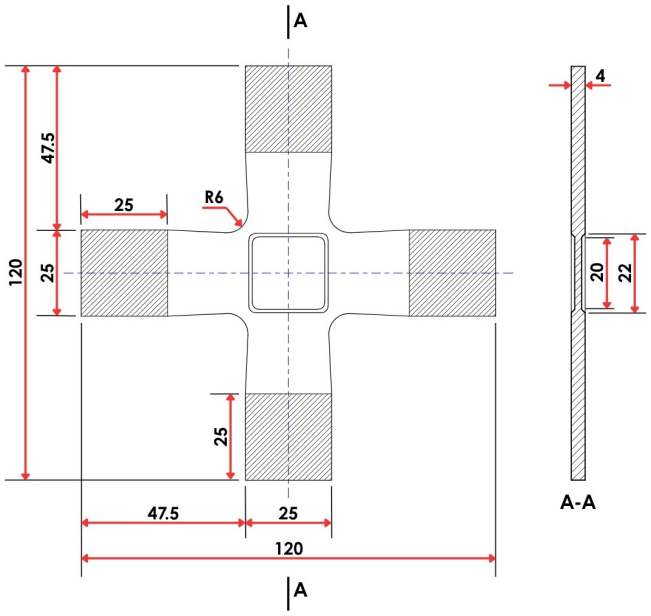


Figure 5. Geometry and A–A cross-section of the initial cruciform specimen (in mm).

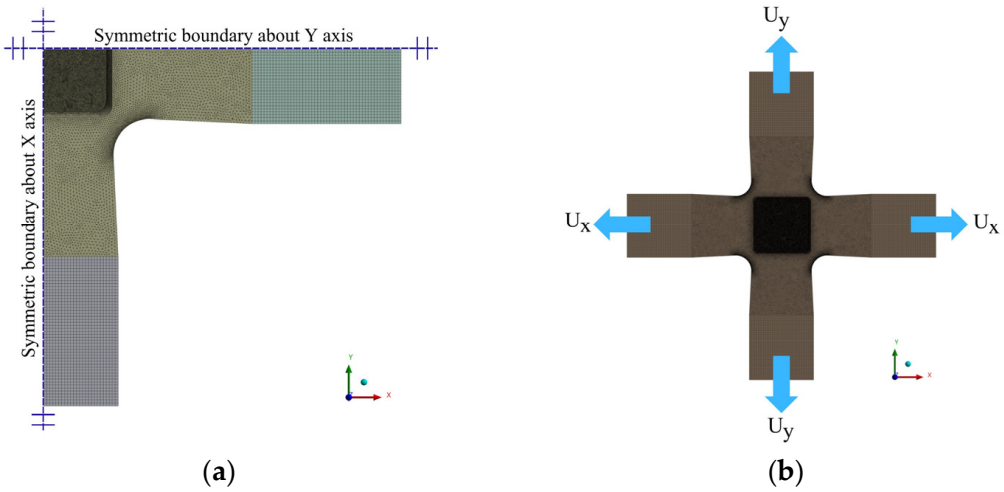


Figure 6. Finite element model of the cruciform specimen (**a**) quarter-model and (**b**) displacement-controlled loading scheme.

To assess the uniformity of stress distribution occurring within the gauge zone, stress data were sampled across a reduced evaluation window that filtered out stress distortions originating from edges. Although the nominal gauge zone had dimensions of 20 × 20 mm (A × A), an inner square effective evaluation area with a side-length ratio of a/A = 0.9, corresponding to 18 × 18 mm (a × a), was used for the quantitative evaluation of stress. This reduced evaluation area was selected to reduce the influence of geometric transitions and to follow the methodology adopted in cruciform specimen shape optimization recommended in the literature. Within this effective gauge zone, the equivalent stress (S_{eqv}), normal stresses S_{11} and S_{22}, and shear stress S_{12} were extracted from the finite element analyses. The effective area considered for stress extraction is illustrated in Figure 7.

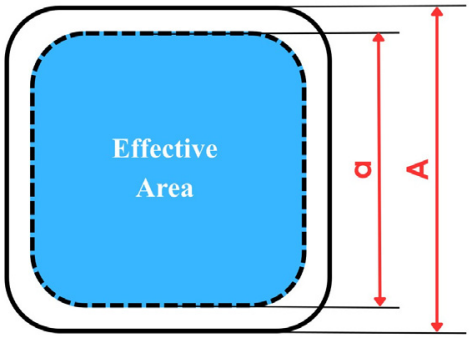


Figure 7. Effective area considered for both average and standard deviation of stresses in the gauge zone.

In the FEM setup, two different analysis objectives were followed in the transfer of material properties: shape optimization and post-shape optimization comparative evaluation. During the shape optimization process of the cruciform specimen, only experimental elastic material property data from a 10 wt% Al microparticle-reinforced epoxy adhesive were used to determine the optimum cruciform specimen geometry. Thus, shape optimization was performed under a single experimentally represented reference-material case, and across all Design of Experiments (DOE) combinations, the material property input was kept constant, with optimization based solely on geometry-dependent stress distribution variations. The geometry was then re-evaluated with additional finite element analyses, and both the initial and optimized geometries were solved separately using both experimental material data and homogenized engineering constants obtained from RVE sizes determined by a statistical worst-case threshold-normalized selection approach. The constants E_1, E_2, E_3, G_{12}, G_{23}, G_{13}, ν_{12}, ν_{23}, and ν_{13} obtained in RVE-based analyses were defined as orthotropic linear elastic models in the ANSYS Mechanical. Therefore, equivalent elastic properties obtained from microstructure-based homogenization analyses were directly transferred to the macro-scale cruciform specimen model.

In addition, comparative stress analyses performed after shape optimization were conducted using the full model rather than the quarter model. This was adopted to allow for a more obvious and holistic evaluation of the effects of orthotropic linear elastic material properties derived from RVEs on cruciform specimen behavior across the whole specimen geometry. Furthermore, using the full model to present and compare the final stress distributions under experimental and RVE-based material definitions for the initial and optimized geometries directly demonstrated the effect of the material definition at the specimen scale, without relying on symmetry reduction.

3.2. Dynamic Machine-Learning-Assisted Global Optimization Framework

In this study, the dynamic XGBoost-MaxLIPOTR-based machine-learning-supported global optimization approach developed by Zhang et al. [21] for turbomachinery blade aerodynamic optimization has been conceptually adopted and adapted to the shape optimization problem of a cruciform specimen geometry. The design vector is x = (R, t), and the design ranges used in this study are defined as follows:

$$R \in [3.00, 12.00] \text{ mm}, t \in [0.25, 3.00] \text{ mm}$$

Biaxial FEA is conducted for each geometry, and the equivalent stress is extracted only for the effective gauge zone. From this zone, two stress uniformity metrics are calculated based on the following objective functions:

(i) Coefficient of variation (CV%) of stress distribution:

$$f_1(R,\ t) = \frac{\sigma_{std}}{\sigma_{mean}} \times 100$$

(ii) Stress range:

$$f_2(R,\ t) = \sigma_{max} - \sigma_{min}$$

These uniformity metrics are then converted into a single composite response function:

$$y(R,t)\ =\ \alpha f_1(R,t) + \beta f_2(R,t), \quad \alpha + \beta\ =\ 1$$

where $\alpha\ =\ 0.5$ and $\beta\ =\ 0.5$. This response function represents the target variable for the XGBoost model throughout the optimization cycle. The optimization cycle begins by generating a fundamental initial design space. The design space is generated using the Latin Hypercube Sampling (LHS) scheme.

XGBoost regression model is trained using the input variables $x_i\ =\ (R_i,\ t_i)$ and the target variable y_i from the database $\{(R_i,\ t_i,\ y_i)\}_{i=1}^{N}$. At each training step, the data set is randomly split into 80% training and 20% validation subsets. The hyperparameter values were kept constant throughout all iterations in the model. Initially, the model was trained using data from only 60 DOE points, and MaxLIPOTR was run on this model to determine the first surrogate optimum in the full design space. This point was verified with a finite element analysis and added to the database.

Two-stage optimization mechanism in the Dynamic XGBoost-MaxLIPOTR-based machine learning model systematically narrows the design space by sequentially applying Lipschitz-based global exploration and trust-region-based local refinement steps at each iteration. In the global exploration phase, the piecewise Lipschitz upper-bound criterion defined by Zhang et al. [21] is applied on the XGBoost regression model trained from the existing design space set. This upper-bound function provides a theoretically valid exploration metric across the entire R-t space and results in the point with the largest bound value being the next candidate solution. Thus, the most promising region on a global scale is determined at each iteration. In the local refinement phase, the trust region approach (TR) in the MaxLIPOTR algorithm is applied. A local quadratic surface is created around the best point identified in the global step, based solely on the surrogate model response. The stationary point of this surface within the TR region is selected as the new local candidate. This process ensures that the optimization process proceeds steadily by refining the direction chosen by the global stage with a more precise local search. Each optimum (R, t) suggested by the model is numerically verified with a single finite element analysis, showing the relative difference between the true objective values y_{real} and the surrogate estimated y_{model} is calculated as

$$e_{fea} = \frac{|y_{model} - y_{real}|}{\max(|y_{real}|, 10^{-12})}$$

On the other hand, the best objective value among all finite element analyses, y_{real}^{best}, is monitored, and the relative improvement in successive iterations is defined as

$$\Delta y_{rel} = \frac{|y_{real}^{best}(k-1) - y_{real}^{best}(k)|}{\max(|y_{real}^{best}(k-1)|, 10^{-12})}$$

The optimization process is terminated when both the relative improvement in the objective function, Δy_{rel}, falls below a predetermined threshold (0.02) and the model-FEA mismatch, e_{fea}, remains below a second threshold (0.20). Thus, convergence is ensured not

only with respect to the model's internal metrics but also in terms of agreement with the FEA results.

In this study, the trust-region window is narrowed anisotropically rather than isotropically at each iteration. In other words, the window is narrowed at different rates in the R and t directions. The window is narrowed more actively in the direction of the design variable that has the greatest impact on the objective function, and more gently in the direction where it is less sensitive. At the surrogate optimum point (R^*, t^*), the local derivatives of the objective function are approximated by the central difference approximation using a small fraction of design space:

$$\left.\frac{\partial y}{\partial R}\right|_{(R^*,\, t^*)}, \qquad \left.\frac{\partial y}{\partial t}\right|_{(R^*, t^*)}$$

The absolute values of the derivate

$$g_R = \left|\frac{\partial y}{\partial R}\right|, \qquad g_t = \left|\frac{\partial y}{\partial t}\right|$$

The sensitivity measures g_R and g_t represent the local sensitivity along the corresponding R and t axes, respectively. The total sensitivity is obtained using $g_{total} = g_R + g_t$, which yields normalized direction weights as follows:

$$w_R = \frac{g_R}{g_{total}}, \qquad w_t = \frac{g_t}{g_{total}}$$

The directional shrinkage of the trust region radii is controlled by shrink factors selected in the range $[s_{min}, s_{max}] = [0.60,\ 0.90]$ as follows:

$$s_R = s_{max} - (s_{max} - s_{min})w_R, \qquad s_t = s_{max} - (s_{max} - s_{min})w_t$$

Thus, in the direction where the objective function is more sensitive (w is larger), the trust region is narrowed more aggressively. The radii in the next iteration are updated as

$$r_R(k+1) = s_R r_R(k), \qquad r_t(k+1) = s_t r_t(k)$$

Later, the corresponding window is updated as follows:

$$R \in [R^* - r_R(k+1), R^* + r_R(k+1)], \qquad t \in [t^* - r_t(k+1), t^* + r_t(k+1)]$$

After each narrowing window, a new LHS-based DOE is created to fill the enhanced area. In case the surrogate is queried for each candidate geometry, the data points within those geometries are added to the database, and the XGBoost model is retrained on the enriched dataset. As the design window shrinks, it transitions from fundamental, global exploration to local exploitation. The dynamic machine-learning-assisted global optimization framework flowchart is shown in Figure 8.

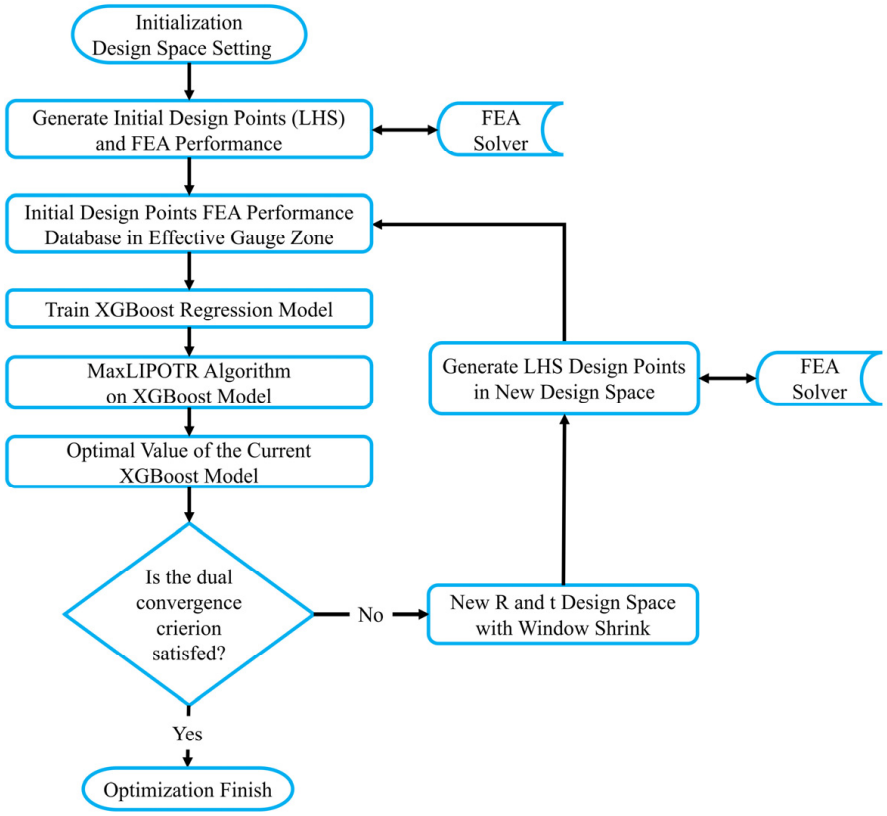


Figure 8. Flowchart of the XGBoost-MaxLIPOTR framework.

4. Results

In this section, the dynamic XGBoost-MaxLIPOTR framework was adapted to the shape optimization problem of the cruciform specimen, and the performance of the selected final design was evaluated considering its results. The near-optimal geometry was selected by examining the convergence characteristics of the initial machine-learning-assisted search. The stress distributions of the initial and optimized geometries were then analyzed, and improvements in the global stress field were reported. In these comparative evaluations, the responses of the initial and optimized geometries were examined separately using the experimentally determined elastic properties and the RVE-predicted homogenized engineering constants for each weight fraction. Finally, the levels and uniformity of stress levels in the effective measurement regions of the initial and optimized geometries were compared under both material definitions, thereby enabling a separate assessment of the geometry optimization effects at the cruciform specimen and at the effective gauge zone.

4.1. Dynamic XGBoost-MaxLIPOTR Framework Performance and Selection Optimized Specimen

In this study, the dynamic XGBoost-MaxLIPOTR framework implemented for the shape optimization problem of the cruciform specimen was evaluated considering the learning dynamics in the final iteration, surrogate-FEA prediction fitting, and convergence order in the design space. The Mean Absolute Error (MAE)-epochs curve at the final iteration in Figure 9a illustrates the surrogate model's learning behavior after it was retrained on the subspace obtained via the dynamic window reduction strategy. The rapid decrease in the validation set errors since the earlier epochs, settling into a low-amplitude, stable plateau, and the consistent decrease in the training error demonstrate that this model can capture the main relationships without overfitting. A well-conditioned generalization capacity was achieved in the final optimization.

Furthermore, the coefficient of determination (R^2) value of 0.8238 calculated in the final iteration validates that the surrogate model can explain a significant portion of the data successfully and can achieve sufficient accuracy to guide the shape optimization. Figure 9b also shows the comparison of the model's predictions and the FEA solutions in the final optimization iteration using a parity plot. In case the predictions of the Design of Experiments (DOE) samples within the narrowing window towards the final iteration are examined, they are clustered around a reference line of 45°, indicating no systematic bias in the surrogate model's predictions. The fact that a large portion of the predictions of these DOE samples fall within an error band of ±10% and ±20% indicates that the model can predict corresponding geometries in an optimal region with high precision.

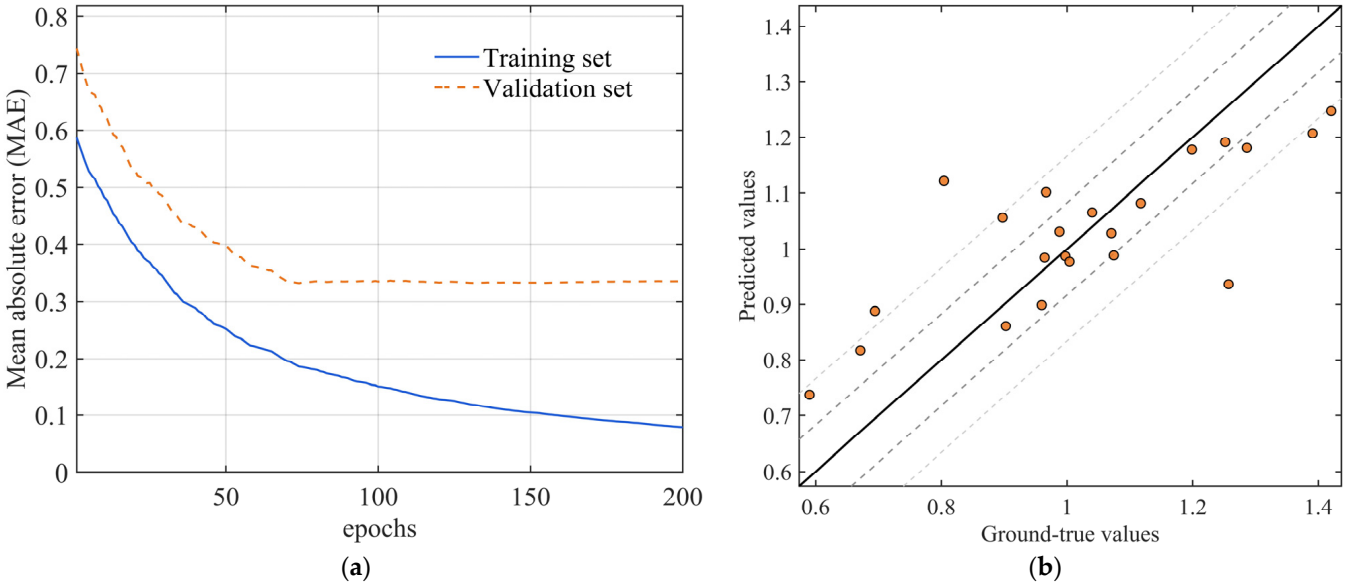


Figure 9. Surrogate model performance evaluated at the final optimization iteration: (**a**) XGBoost training convergence, and (**b**) prediction accuracy versus FEA results.

Figure 10 shows that the distribution of DOEs gradually narrows the search space to a smaller region with each successive iteration during the dynamic window-narrowing process, and that the localization of the optimal geometry becomes more pronounced within this region, where design examples are clustered. Based on the FEA results performed throughout the optimization process, the optimal geometry achieving the lowest objective function value was of a fillet radius (R) of 11.5765 mm and a center thickness (t) of 2.983 mm. This geometry was defined as the "global optimum of FEAs". In the final iteration, the surrogate optimum determined by the MaxLIPOTR algorithm, with a fillet radius (R) of 11.5909 mm and a center thickness (t) of 2.9442 mm, is close to the optimum of FEAs. This slight difference confirms that the surrogate model can capture the optimum region with high accuracy. Consequently, the minor differences between the true optimum of FEAs and the surrogate optimum values indicate that the double convergence criterion is met properly.

The design parameters R = 11.5 mm and t = 3 mm were selected for the optimized candidate geometry of the cruciform specimen, considering not only the numerical results but also the manufacturability of the optimized specimen.

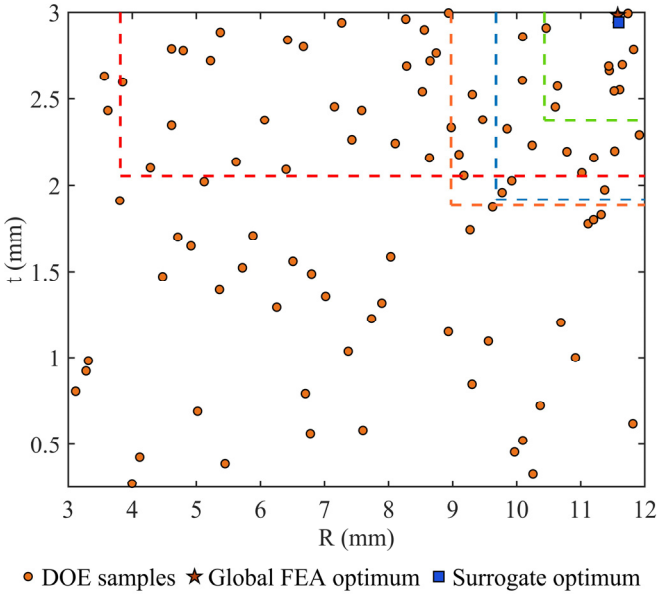


Figure 10. Successive contraction of the design space (R-t) under the dynamic update strategy. The colored dashed lines indicate the boundaries of the updated design-space windows during successive contractions.

4.2. Stress Distributions in the Initial and Optimized Geometries

This section examines the equivalent stress (S_{eqv}) distributions of the full initial and optimized cruciform specimens in order to clarify the effect of the proposed geometric modification on the overall stress transfer behavior. The comparison is performed using both the experimentally determined elastic properties and the RVE-predicted engineering constants for each weight fraction so that the response of the optimized candidate geometry can be assessed under the two material descriptions considered in this study. Particular attention is given to the fillet transition regions and the central gauge zone, since these regions directly reflect the severity of stress concentration and the quality of the stress field established in the effective gauge zone. In this context, the stress distributions are evaluated with respect to whether the optimized candidate geometry reduces stress accumulation around the fillet radius and promotes a more stable and homogeneous equivalent stress field within the gauge zone.

4.2.1. Comparisons Based on Experimental Elastic Properties

As shown in Figure 11, the initial cruciform geometry exhibited pronounced equivalent stress localization at the fillet transition region for all materials, with peak values of 12.120 MPa, 12.951 MPa, and 13.023 MPa for the 2, 6, and 10 wt% aluminum microparticle-reinforced epoxy adhesives, respectively. This concentration restricted effective stress transfer toward the central gauge region and was accompanied by noticeable heterogeneity in the gauge zone stress field, where the mean Seqv values were 6.469 MPa, 6.912 MPa, and 6.951 MPa, with corresponding standard deviations of 0.133 MPa, 0.142 MPa, and 0.143 MPa. Following the shape optimization, the fillet region peak stresses decreased markedly to 8.513 MPa, 9.097 MPa and 9.148 MPa, respectively, indicating that the optimized candidate geometry substantially relieved local stress buildup in the transition zones. More importantly, the gauge zone standard deviation was reduced to 0.061 MPa, 0.066 MPa, and 0.066 MPa, demonstrating a clear improvement in stress uniformity. The results confirm that, when evaluated using the experimental elastic properties, the optimized candidate geometry provides a substantially more homogeneous equivalent stress distribution within the effective gauge zone than the initial geometry.

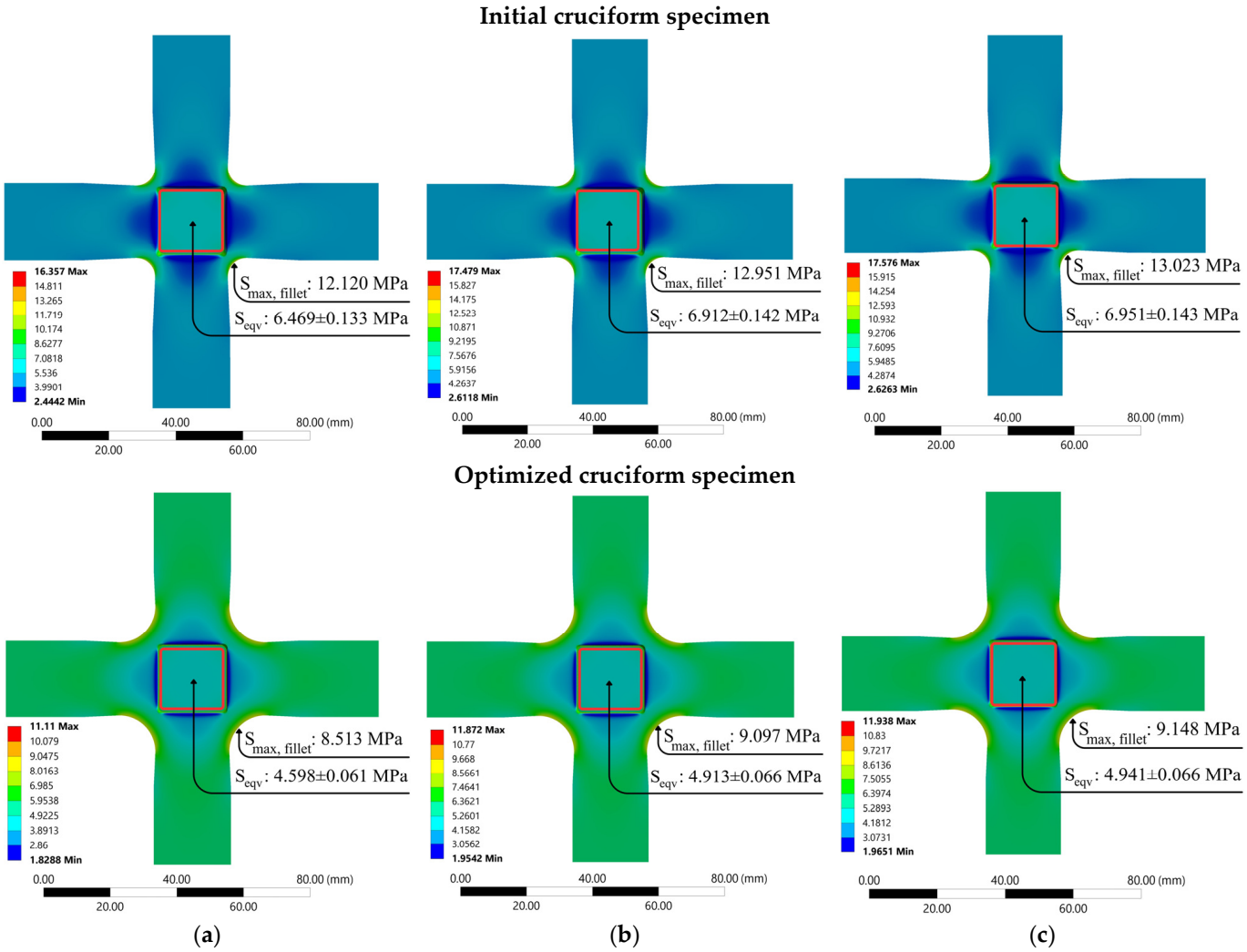


Figure 11. Equivalent stress S_{eqv} distributions of the initial and optimized cruciform specimens based on the experimental elastic properties for (**a**) 2 wt%, (**b**) 6 wt%, and (**c**) 10 wt% aluminum microparticle-reinforced epoxy adhesives.

4.2.2. Comparisons Based on RVE-Predicted Engineering Constants

A similar distribution pattern was obtained when the material response was described by the RVE-predicted engineering constants, as illustrated in Figure 12. In the initial geometry, the highest equivalent stresses again developed around the fillet transition region, reaching 12.216 MPa, 12.679 MPa, and 13.169 MPa for the 2, 6, and 10 wt%, respectively. Within the gauge zone, the corresponding mean Seqv values were 6.517, 6.760, and 7.017 MPa, while the standard deviations remained relatively high at 0.134, 0.139, and 0.145 MPa, indicating that the non-uniform stress transfer character of the initial geometry persisted under the RVE-based material definition as well. Following shape optimization, the peak fillet stresses decreased to 8.579, 8.903, and 9.246 MPa, respectively, while the gauge zone standard deviations fell to 0.062, 0.064, and 0.067 MPa. Therefore, the RVE-based results reproduce the same fundamental outcome observed with the experimental properties: the optimized candidate geometry suppresses stress accumulation at the fillet transition and establishes a distinctly more stable and homogeneous equivalent stress field in the central gauge region.

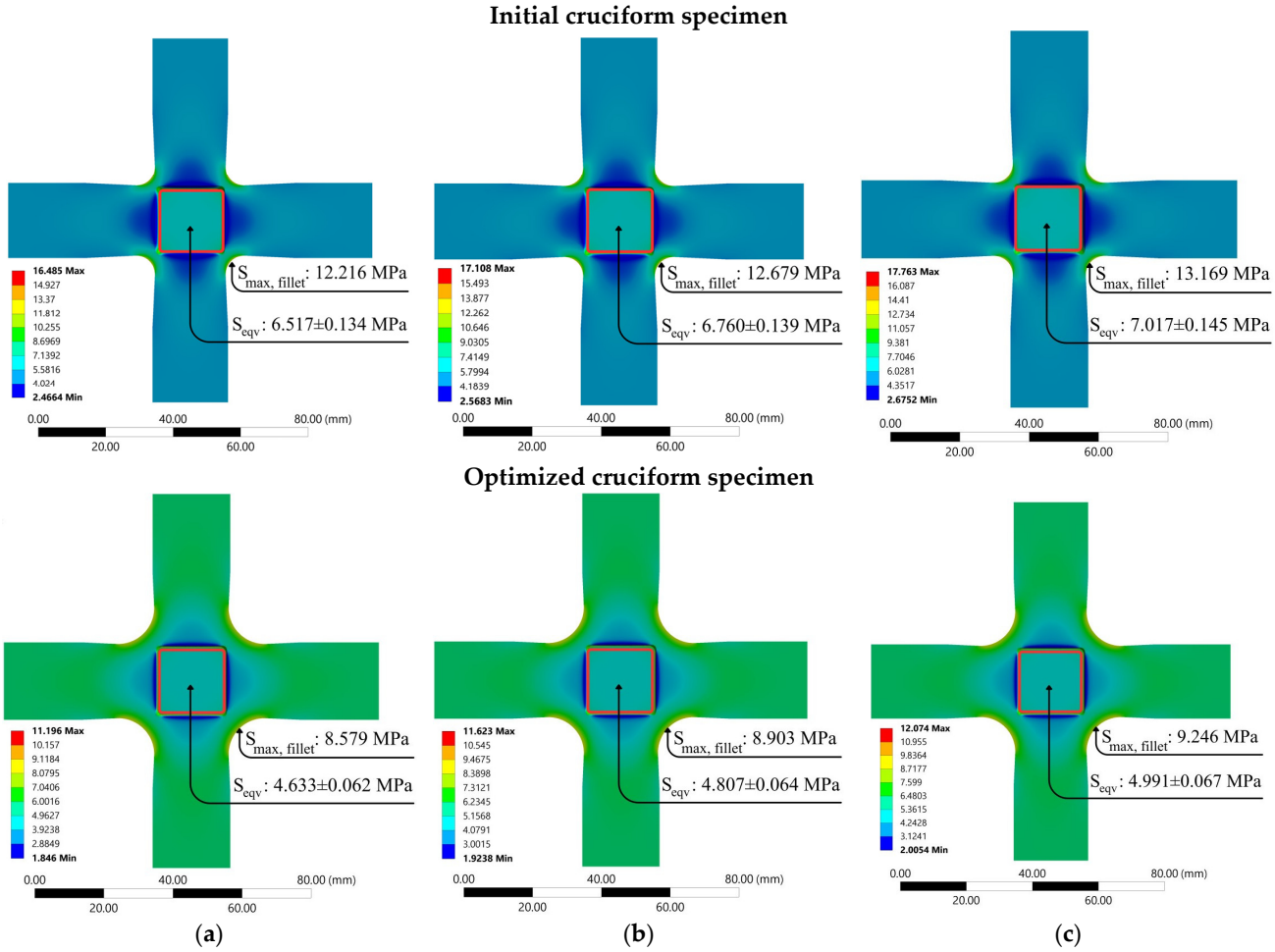


Figure 12. Equivalent stress S_{eqv} distributions of the initial and optimized cruciform specimens based on the RVE-predicted engineering constants' properties for (**a**) 2 wt%, (**b**) 6 wt%, and (**c**) 10 wt% aluminum microparticle-reinforced epoxy adhesives.

4.3. Stresses in Gauge Zone

The stress fields within the gauge zone were evaluated for the initial and optimized cruciform geometries in order to assess how effectively the proposed shape modification improved the uniformity of the elastic stress state in the central test region. The analysis considers both the experimentally determined elastic properties and the RVE-predicted engineering constants, and includes the equivalent stress (S_{eqv}), normal stress (S_{11}/S_{22}), and shear stress (S_{12}) distributions. For this purpose, isoline maps were interpreted together with the corresponding mean μ and standard deviation σ values calculated over the effective gauge zone defined previously in Figure 7, thereby excluding the fillet-affected transition regions from the comparison. To ensure a consistent visual interpretation, fixed contour intervals were adopted for each stress component, namely, 0.032 MPa for S_{eqv} and 0.1 MPa for both S_{11}/S_{22} and S_{12}. Due to the minimal standard deviation in the gauge zone, the optimized candidate geometry exhibits better stress homogeneity. Under this framework, closer isoline spacing indicates stronger local stress gradients, whereas smoother and more regularly spaced contours indicate a more homogeneous stress distribution within the gauge zone. In addition, the a/A-based results are used to quantify how the stress homogeneity evolves with the effective gauge zone ratio.

4.3.1. Gauge Zone Results Based on Experimental Elastic Properties

As shown in Figure 13, the optimized candidate geometry establishes a distinctly more uniform S_{eqv} field within the gauge zone than the initial geometry. In the initial geometry, the contour lines are concentrated more strongly toward the corner regions of the gauge zone, indicating that the equivalent stress varies more rapidly as the boundary of the effective gauge zone is approached. By contrast, the optimized specimen exhibits a broader low gradient central region and a more regular outward contour development for all three materials. This visual change is fully consistent with the statistical results, since the standard deviation decreases from 0.133, 0.142, and 0.143 MPa in the initial geometry to 0.061, 0.066, and 0.066 MPa in the optimized candidate geometry for the 2, 6, and 10 wt%, respectively. These results confirm that the proposed geometric optimization substantially improves the homogeneity of the equivalent stress distribution within the gauge zone when the experimentally determined elastic properties are used.

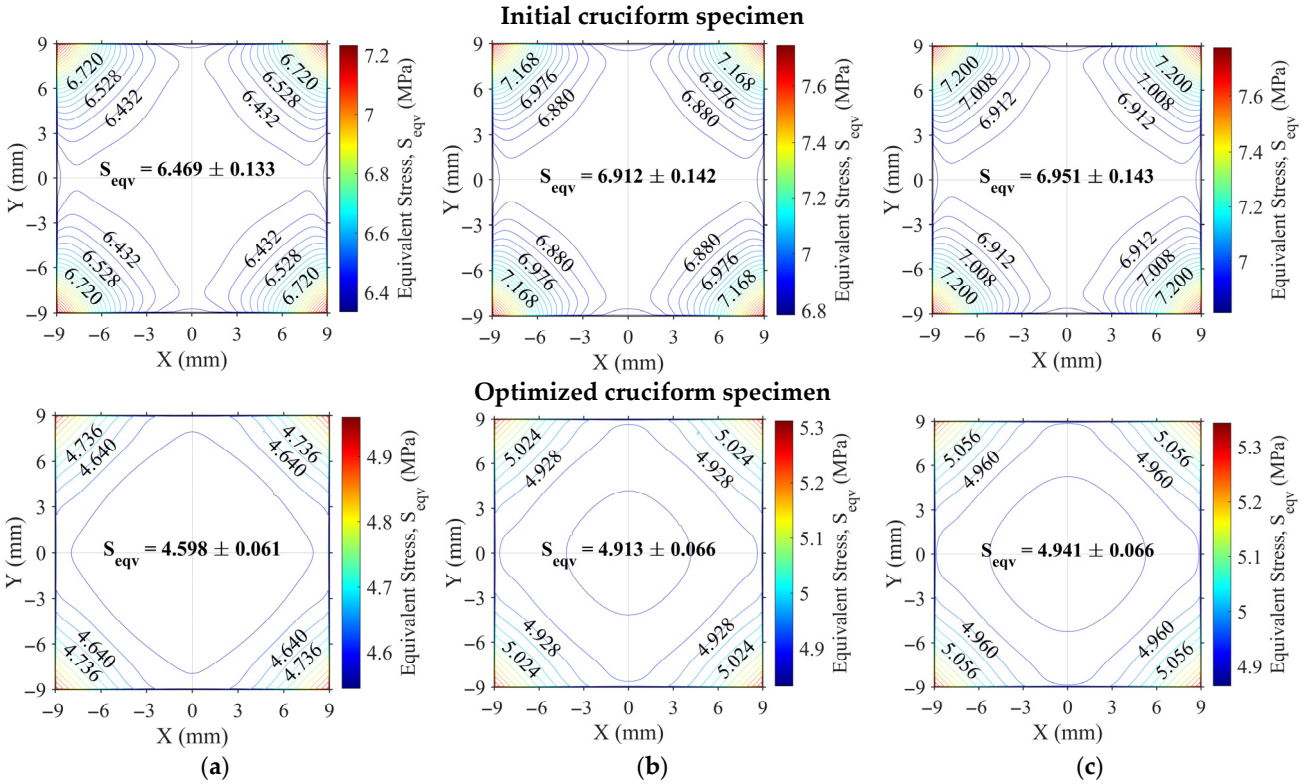


Figure 13. Equivalent stress S_{eqv} distributions in the gauge zones of the initial and optimized cruciform specimens based on the experimental elastic properties for (**a**) 2 wt%, (**b**) 6 wt% and (**c**) 10 wt% aluminum microparticles.

Since the normal stress S_{11} and S_{22} isolines are symmetrical along an angle of 45 degrees with respect to the origin, only the isoline graph of S_{11} is shown (Figure 14). The normal stress S_{11} isoline distributions of the initial geometry exhibit sharp transitions from the center outward, whereas this does not happen for those of the optimized candidate geometry. In the optimized candidate geometry, these transitions are less frequent and have a smoother gradient. Furthermore, the standard deviation values decreased from 0.286 MPa, 0.306 MPa, and 0.307 MPa in the initial geometry to 0.211 MPa, 0.225 MPa, and 0.227 MPa in the optimized candidate geometry for the 2, 6, and 10 wt%, respectively. This demonstrates the improved homogeneity of the stress distributions in the biaxial tensile directions in the optimized candidate geometry.

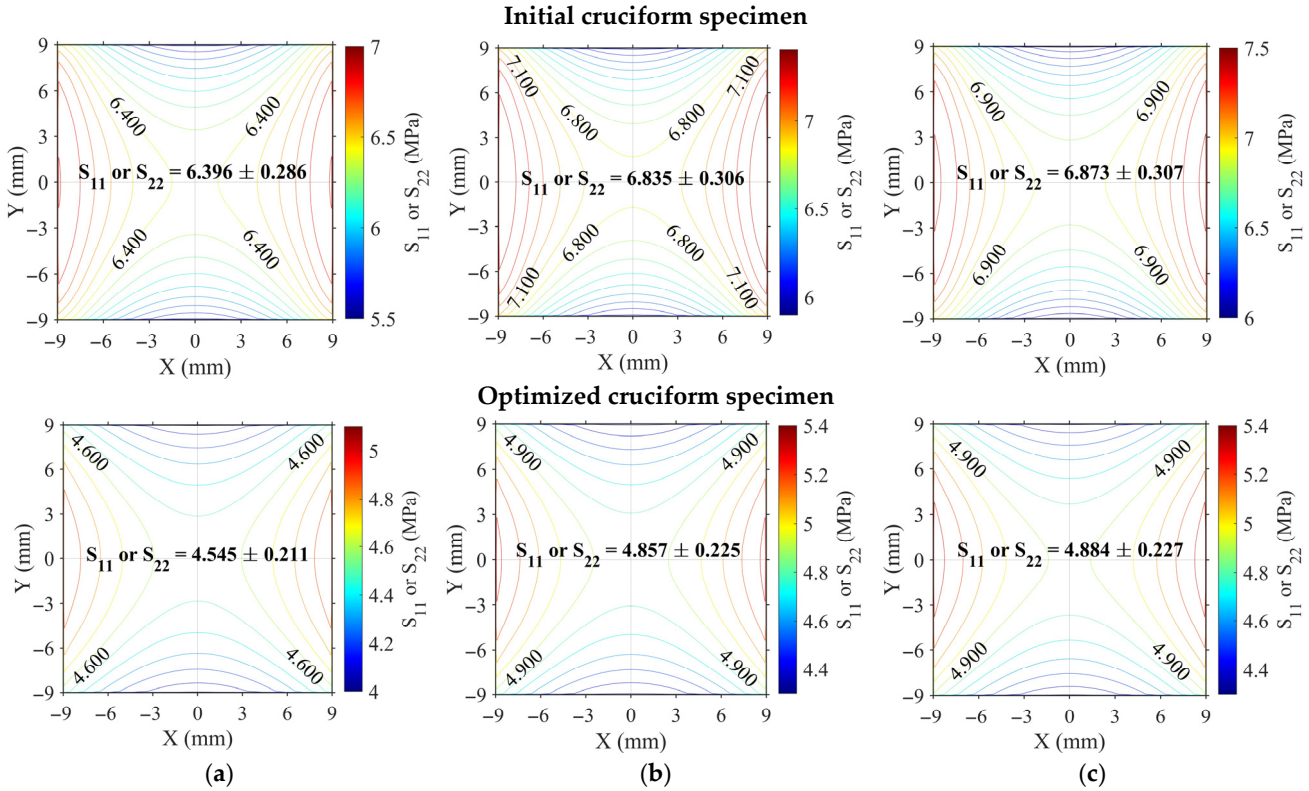


Figure 14. Normal stress S_{11} or S_{22} distributions in the gauge zones of the initial and optimized cruciform specimens based on the experimental elastic properties for (**a**) 2 wt%, (**b**) 6 wt% and (**c**) 10 wt% aluminum microparticles.

A comparable improvement is observed for the shear stress distributions in Figure 15. In the initial geometry, the S_{12} contours display stronger directional variation across the diagonal regions of the gauge zone, revealing a less balanced shear stress pattern. After optimization, the contour field becomes smoother and more symmetrically distributed, indicating that the geometric optimization reduces shear stress irregularity within the central gauge region. Quantitatively, the standard deviation decreases from 0.490, 0.524, and 0.527 MPa in the initial geometry to 0.343, 0.366, and 0.368 MPa in the optimized candidate geometry for the 2, 6, and 10 wt%, respectively. This corresponds to an approximately 30% reduction in shear stress dispersion, demonstrating that the optimized candidate geometry also improves the symmetry and stability of the biaxial load transfer with respect to the shear component.

The evolution of stress homogeneity with increasing effective gauge zone ratio is further quantified in Figure 16. For all three weight fractions, the optimized candidate geometry consistently exhibits lower standard deviation values than the initial geometry for Seqv, S_{11}/S_{22}, and S_{12}, and this difference becomes more pronounced as the evaluated gauge zone region expands. This behavior indicates that the initial geometry is increasingly affected by boundary-driven stress heterogeneity when a larger portion of the gauge zone is considered, whereas the optimized candidate geometry preserves a more stable stress field over a wider region. The corresponding uniformity improvement reaches approximately 40.32–54.98% for equivalent stress, 11.20–30.72% for the normal stresses, and 11.34–32.30% for the shear stresses. Accordingly, the optimized specimen does not merely improve stress regularity near the center but maintains this homogenization effect throughout a broader effective gauge zone.

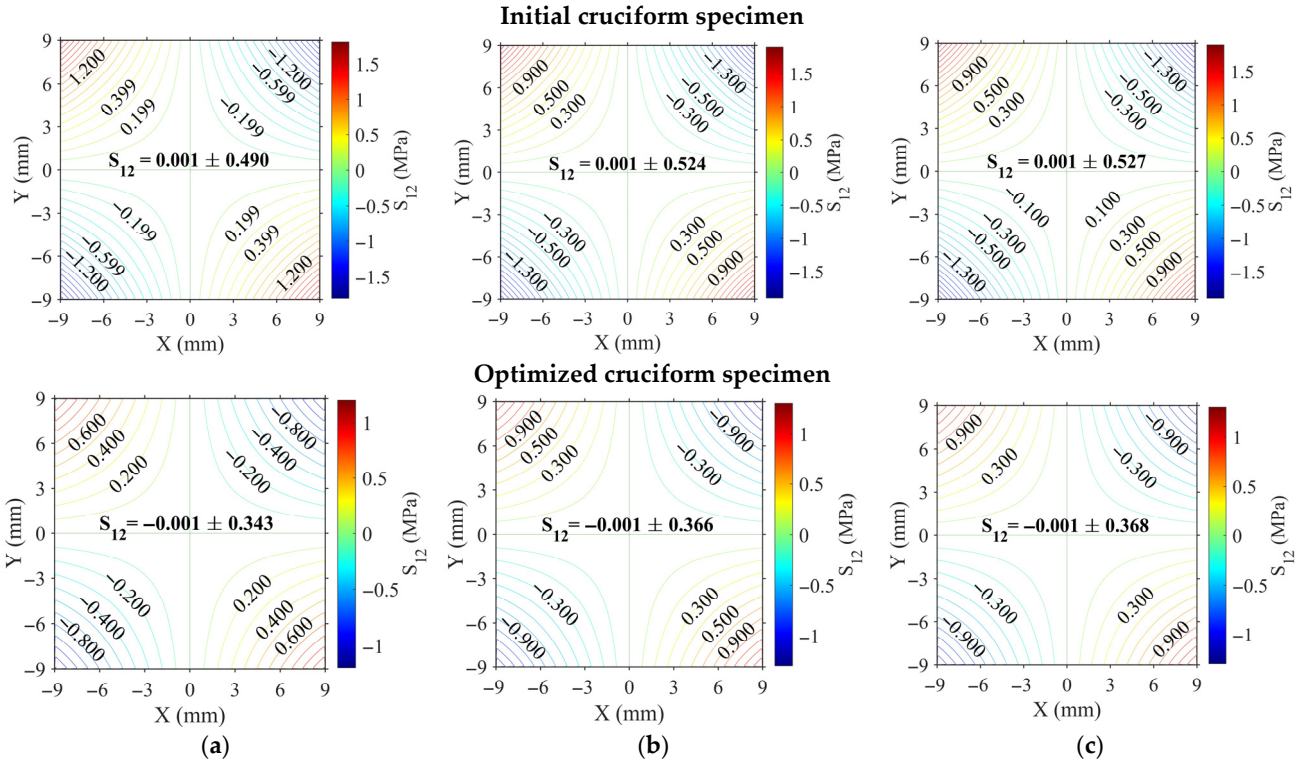


Figure 15. Shear stress S_{12} distributions in the gauge zones of the initial and optimized cruciform specimens based on the experimental elastic properties for (**a**) 2 wt%, (**b**) 6 wt% and (**c**) 10 wt% aluminum microparticles.

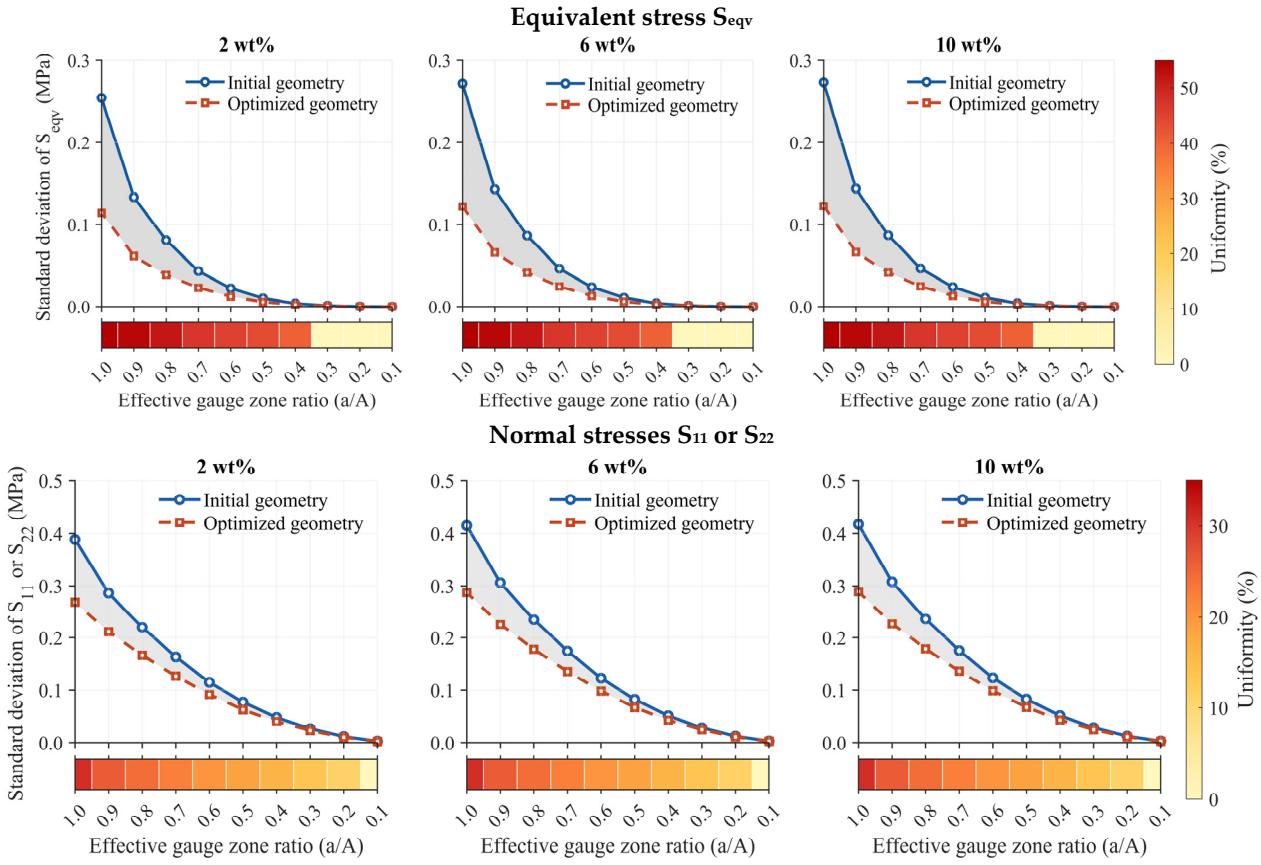


Figure 16. *Cont.*

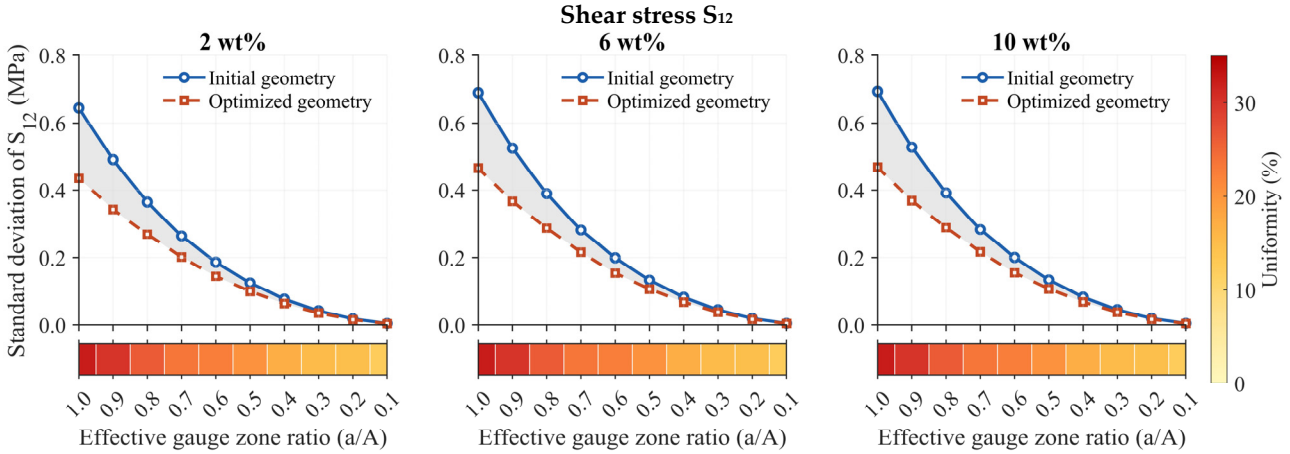


Figure 16. Variations in the standard deviation σ and the corresponding uniformity (%) values with effective gauge zone ratio (a/A) for equivalent, normal, and shear stresses in the initial and optimized cruciform geometries, based on the experimental elastic properties, for the 2, 6, and 10 wt%.

4.3.2. Gauge Zone Results Based on RVE-Predicted Engineering Constants

The same overall behavior is preserved when the material response is defined using RVE-predicted engineering constants. As seen in Figure 17, the optimized candidate geometry again yields a more regular and spatially uniform Seqv field within the gauge zone, whereas the initial geometry retains a stronger corner-dominated contour concentration and more pronounced local variation. In the optimized candidate geometry, the central region becomes more weakly graded and the outward contour progression becomes smoother for all three weight fractions. This is supported by the statistical results, where the standard deviation decreases from 0.134, 0.139, and 0.145 MPa in the initial geometry to 0.062, 0.064, and 0.067 MPa in the optimized candidate geometry for the 2, 6, and 10 wt%, respectively. Thus, the homogenization effect observed for the experimentally determined elastic properties is also reproduced under the RVE-based material description.

Since the normal stress S_{11} and S_{22} isolines are symmetrical with respect to the 45-degree direction through the origin, only the isoline graph of S_{11} is presented in Figure 18. In the initial geometry, the S_{11} contours display more abrupt changes from the center toward the outer regions, reflecting stronger local gradients. By comparison, the optimized candidate geometry shows smoother and more gradual contour transitions for all three materials. Furthermore, the standard deviation values decreased from 0.288 MPa, 0.299 MPa, and 0.311 MPa in the initial geometry to 0.213 MPa, 0.221 MPa, and 0.229 MPa in the optimized candidate geometry for the 2, 6, and 10 wt%, respectively. This indicates that the optimized candidate geometry preserves its ability to improve the homogeneity of the normal stress distributions along the biaxial tensile directions under the RVE-predicted engineering constants definitions.

Figure 19 shows that the shear stress S_{12} field changes progressively from the specimen arms towards the gauge zone. Relative to the initial geometry, the optimized candidate geometry exhibits a smoother and more uniformly distributed transition of shear stress towards the fillet zone. This trend is also reflected in the statistical results, where the standard deviation decreases from 0.494 MPa, 0.514 MPa, and 0.534 MPa in the initial geometry to 0.345 MPa, 0.358 MPa, and 0.372 MPa in the optimized candidate geometry for the 2, 6, and 10 wt%, respectively. In addition, this corresponds to approximately 30% reduction in the standard deviation relative to the initial geometry, confirming the improved uniformity of the shear stress distributions. This also suggests that the optimized candidate geometry retains its beneficial effect on reducing shear stress non-uniformity

and promoting a more symmetrical biaxial load transfer when the material behavior is described by the RVE-predicted engineering constants.

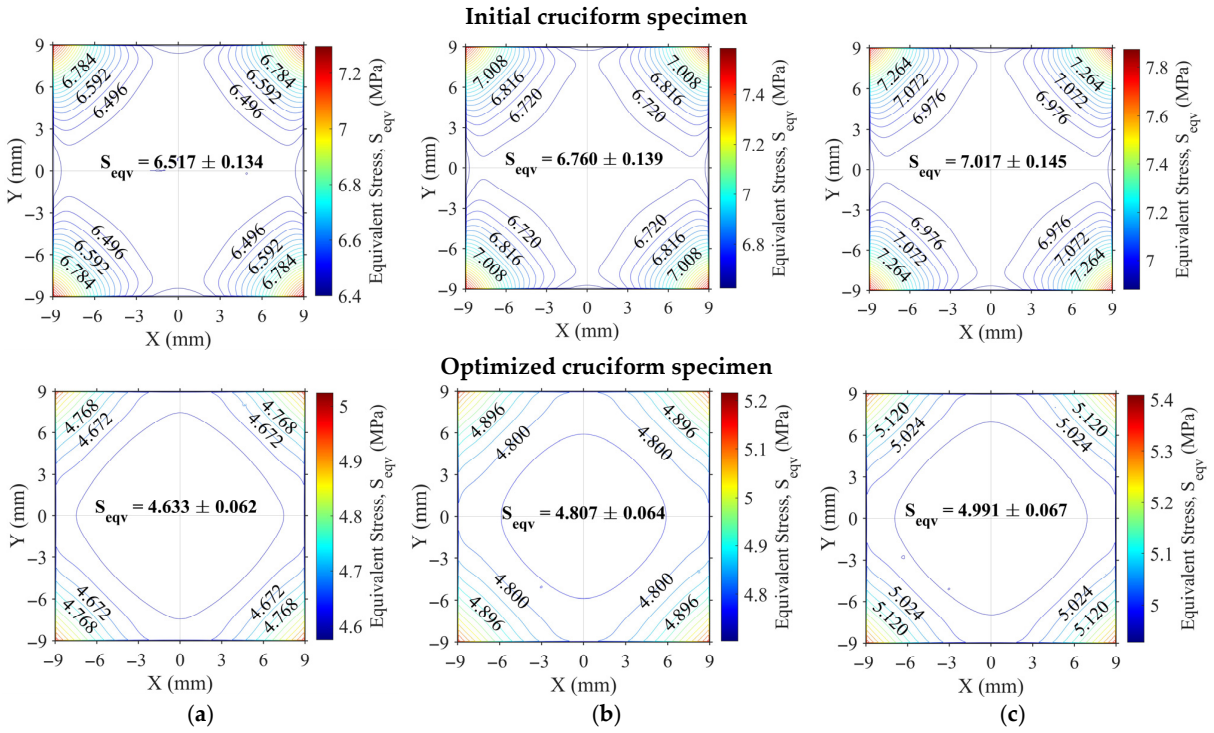


Figure 17. Equivalent stress S_{eqv} distributions in the gauge zones of the initial and optimized cruciform specimens based on the RVE-predicted engineering constants for (**a**) 2 wt%, (**b**) 6 wt% and (**c**) 10 wt% aluminum microparticles.

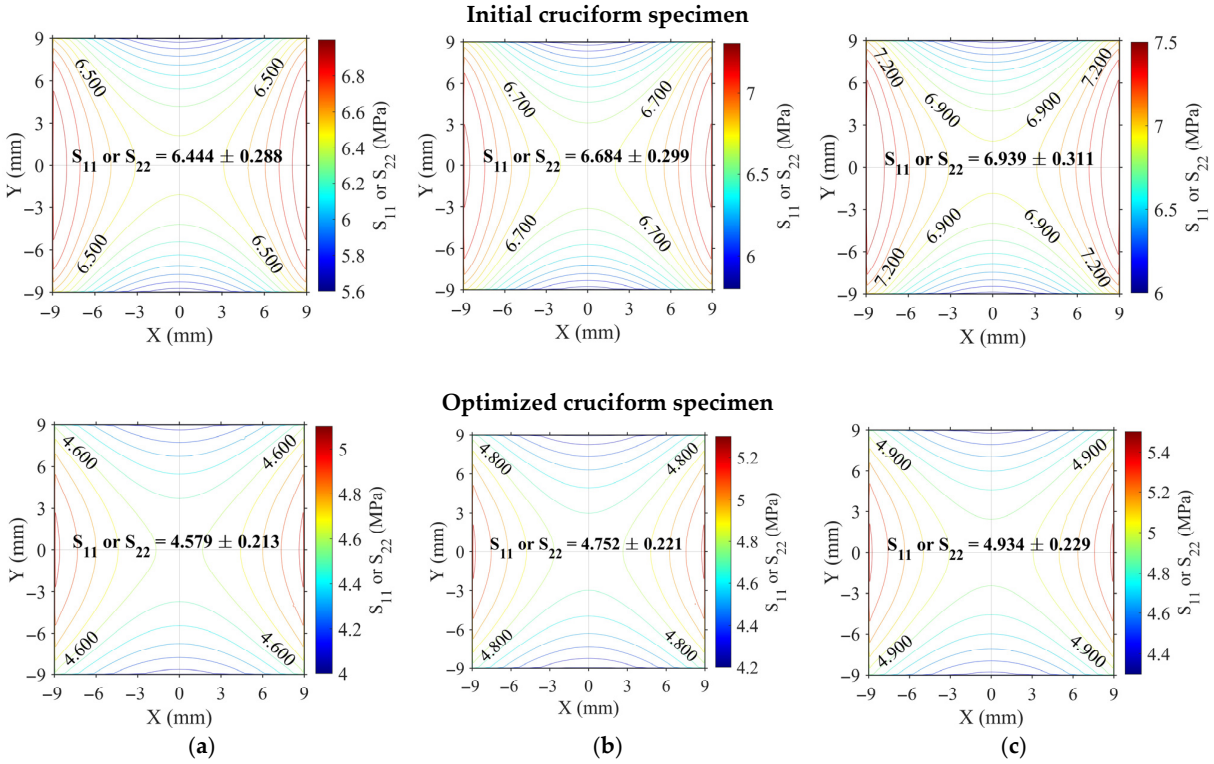


Figure 18. Normal stress S_{11} or S_{22} distributions in the gauge zones of the initial and optimized cruciform specimens based on the RVE-predicted engineering constants for (**a**) 2 wt%, (**b**) 6 wt% and (**c**) 10 wt% aluminum microparticles.

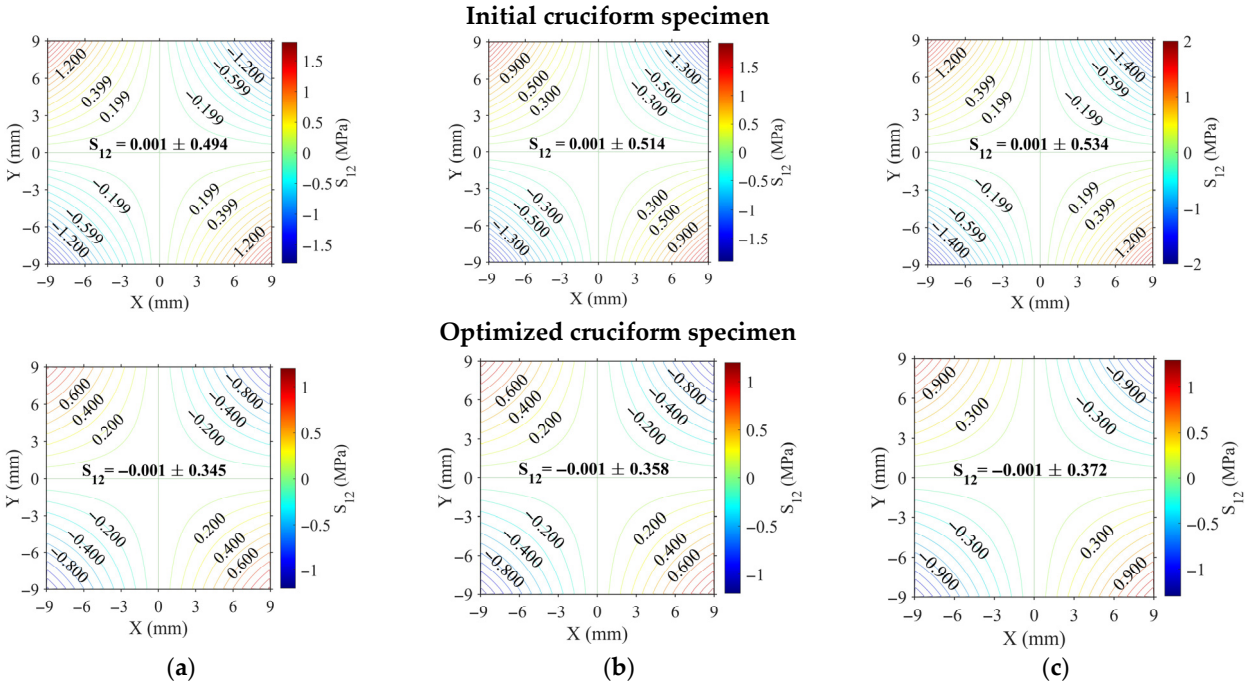


Figure 19. Shear stress S_{12} distributions in the gauge zones of the initial and optimized cruciform specimens based on the RVE-predicted engineering constants for (**a**) 2 wt%, (**b**) 6 wt% and (**c**) 10 wt% aluminum microparticles.

Figure 20 further demonstrates that the advantage of the optimized candidate geometry is maintained over the full range of effective gauge zone ratios investigated. For all three stress measures and for all three materials, the optimized candidate geometry remains below the initial geometry in terms of standard deviation, while the associated uniformity values remain consistently higher. As in the experimental property-based results, the difference between the two geometries becomes more evident as the effective gauge zone ratio increases, indicating that the optimized specimen is less sensitive to the progressive inclusion of regions affected by stronger stress gradients. The uniformity improvement reaches approximately 43.48–54.51% for equivalent stress, 14.31–31.12% for the normal stress, and 12.50–34.07% for the shear stress. Taken together, these results confirm that the proposed geometric optimization provides a robust improvement in gauge zone stress homogeneity, regardless of whether the material properties are introduced directly from the experiment or through the RVE-predicted engineering constants.

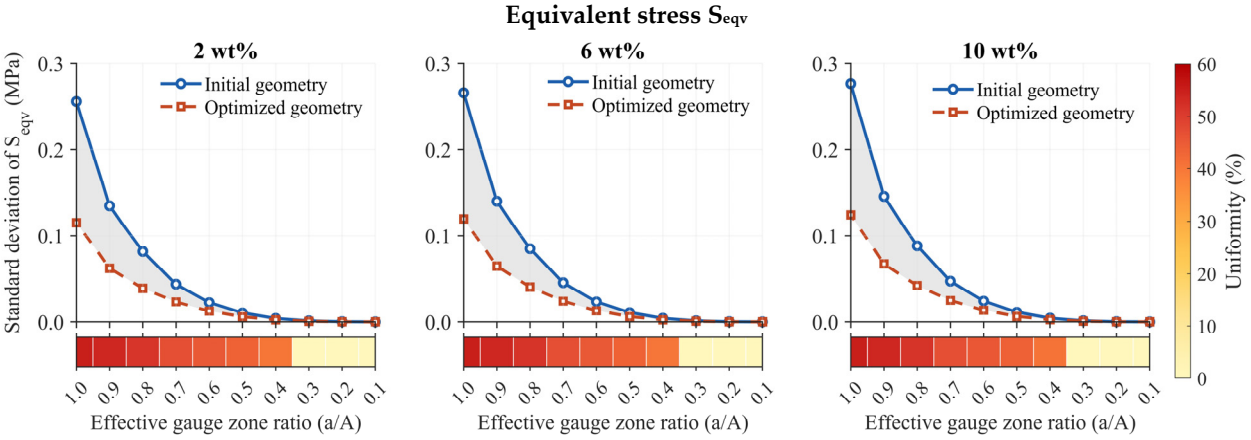


Figure 20. *Cont.*

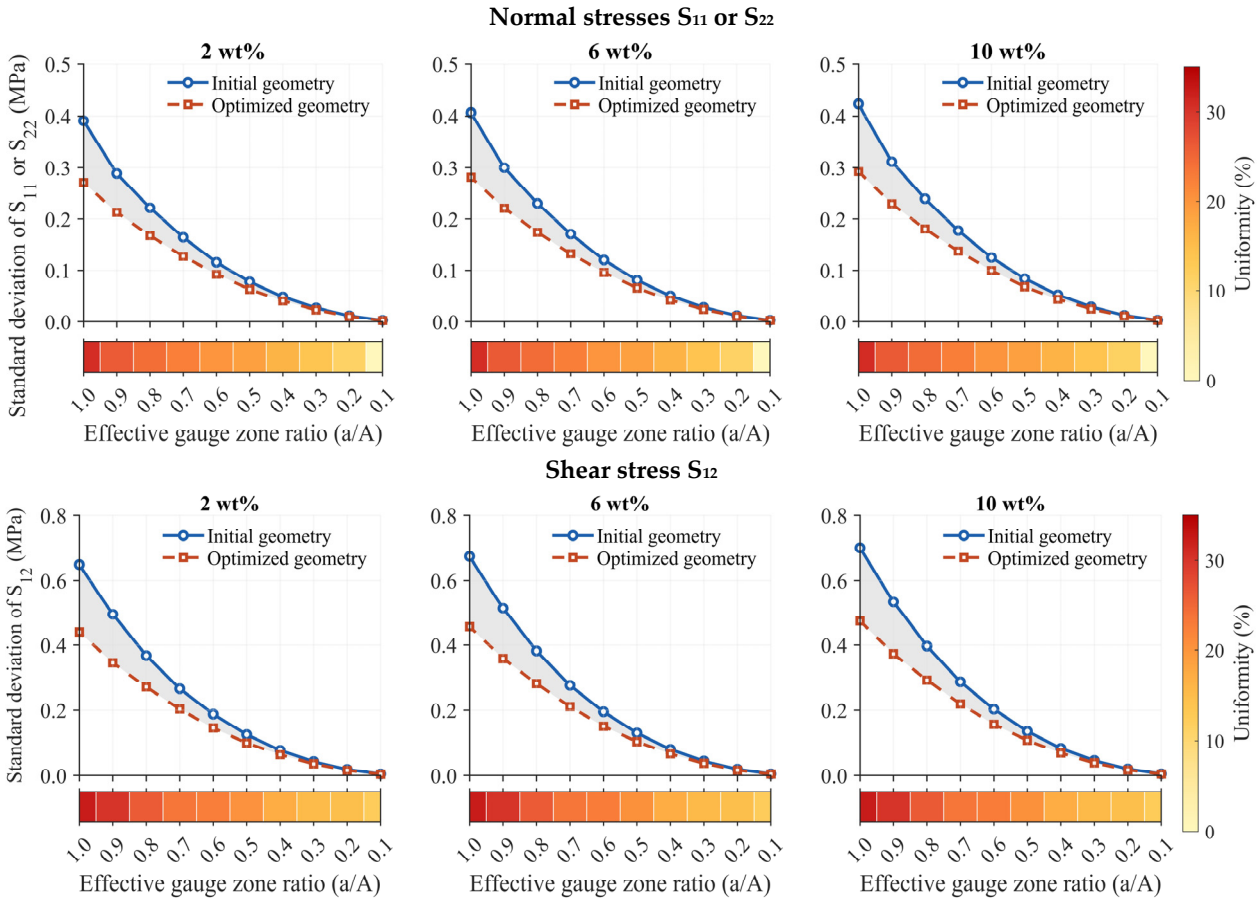


Figure 20. Variations in the standard deviation σ and the corresponding uniformity (%) values with effective gauge zone ratio (a/A) for equivalent, normal, and shear stresses in the initial and optimized cruciform geometries, based on the RVE-predicted engineering constants, for the 2, 6, and 10 wt%.

4.4. Discussion

This study focuses on the optimization of the cruciform specimen geometry using a multiscale approach to reliably assess the in-plane biaxial mechanical behavior of a microparticle-reinforced epoxy-based adhesive. The accuracy of the material properties was verified by comparing the RVE-based micromechanical analyses with the results of uniaxial tensile tests. The mean elastic moduli exhibited low relative errors. The proximity among the directional elastic constants indicates that the directional dependency of the elastic modulus is negligible due to the random microparticle distribution. This validation enabled us to transfer the experimentally determined material parameters into the shape optimization analyses of the cruciform specimen and to considerably reduce material-related uncertainties. The shape optimization analyses were performed using only the experimentally determined elastic properties of the 10 wt% aluminum microparticle-reinforced epoxy adhesive, which was selected as the validated reference material. After the optimized candidate geometry had been identified, the selected RVE-predicted engineering constants were additionally used for the 2, 6, and 10 wt% materials to compare the initial and optimized geometries under a homogenized material description. In this manner, the multiscale framework was implemented as a partially coupled strategy. The macroscopic shape optimization was driven by the experimentally derived effective material property set, maintaining a direct link to the experimentally characterized adhesive response and isolating the influence of specimen geometry on stress homogenization. The RVE-based material definitions were not directly embedded in the active optimization loop; instead, they were used as a complementary post-optimization verification step to assess whether

the stress-homogenization capability of the optimized candidate geometry was preserved across different weight fractions.

The RVE models were formulated using spherical Al microparticles and perfect bonding between matrix and particles to establish a controlled micromechanical representation of the reinforced adhesive microstructure. This idealized representation is suitable for evaluating the effective elastic response within the homogenization framework adopted in this study. However, the local response of practical microparticle-reinforced adhesive systems may also be influenced by interfacial degradation, particle–matrix separation, or deviations from spherical particle morphology, particularly at higher strain levels. Such effects can modify local stress transfer and stress concentrations and may therefore be considered in extended RVE formulations involving imperfect interfaces or more realistic particle geometries.

A significant portion of the related published studies on the optimization of cruciform geometry have indicated that the stress homogeneity is associated with specific design variables, such as fillet radius, center taper, arm width, and slot geometry. It was concluded mainly that the geometric continuity in the load-transfer path may decisively direct the stress field in the gauge zone. Local stress concentrations, particularly at fillet transitions, are generally reported as limiting homogeneity. These studies have also focused on metallic, elastomer, or fiber-reinforced composite materials [9,10,30,31]. The evaluation of the cruciform geometry of a microparticle-reinforced epoxy-based adhesive has received more limited attention. From this perspective, the present study contributes to the existing cruciform specimen optimization literature not only by considering a microparticle-reinforced epoxy adhesive but also by examining the performance of the optimized candidate geometry under both experimentally determined and RVE-predicted material descriptions. This combined assessment provides additional support for the robustness of the geometry-related conclusions with respect to the constitutive representation adopted for the material.

In this context, the present optimization should be interpreted as a manufacturability-constrained shape optimization conducted within a reduced R–t design space. Although arm width, taper profile, slit/slot geometry, and gauge-zone shape may also influence stress homogeneity, stress concentration, and failure localization, varying these parameters would modify the global load-transfer path, fixture compatibility, and mold design. Therefore, the present approach complements richer parametric and topology-optimization studies by focusing on two geometric variables that can be adjusted without changing the external specimen layout or the adopted manufacturing route.

The dynamic XGBoost-MaxLIPOTR-based algorithm was implemented for optimization purposes, and its structure was adapted to the current problem [21]. In this study, the sampling window was narrowed at each iteration based on the effects of the geometric variables R and t. This made the dynamics of window narrowing more sensitive to the variables that most significantly affect stress homogeneity. As the structure of Zhang's original algorithm is preserved [21], a specific directionality was introduced for the shape optimization of the cruciform specimen. This is consistent with the previous studies since it shows that the design parameters, such as the fillet radius and center thickness, affect the load-transfer path.

The agreement between the surrogate model (XGBoost) and the FEA results is improved at each iteration, and in the final optimization iteration, the surrogate model's near-optimal candidate geometry was in good agreement with the optimal geometry derived from the finite element analyses. The reduced discrepancy between the predictions of both the surrogate model and finite element analyses, enabled by the dynamic sampling structure in the Zhang approach, brought the dual convergence criterion to be satisfied. This also confirms that the surrogate model can produce a stable convergence behavior

on the shape optimization problem. The finite accuracy of the surrogate model and the manufacturability-based adjustments to R and t may affect the exact location of the optimum within the investigated design space. Therefore, the selected geometry is interpreted as a near-optimal design within the R–t space considered.

Comparing the initial and optimized candidate shapes, it was observed that the standard deviation in the equivalent stresses in the effective gauge zone was significantly reduced. This reduction in stress distribution is consistent with distribution-based homogeneity metrics used in cruciform specimen evaluations, such as the coefficient of variation in the central gauge zone. Since the coefficient of variation represents a normalized measure of field distribution, the reduction in the contour-based stress-spread measure indicates an improvement in gauge zone stress homogeneity that is qualitatively consistent with CV-type evaluations. In addition, the reduced stress concentration in the cross-arm transition regions is consistent with the design rationale of failure-location- or failure-ratio-based assessments, where a desirable cruciform geometry should promote a more uniform central field while reducing premature localization outside the gauge region [9,10,30,31].

The selected center thickness and reduced transitions in the fillet zones allowed for a more balanced direction of load transfer from the arm zones to the gauge zone. Furthermore, the subsequent comparisons performed using the selected RVE-predicted engineering constants for the 2, 6, and 10 wt% materials showed that the beneficial effect of the optimized candidate geometry was preserved under all investigated material descriptions. The fact that the reductions in stress concentration and gauge zone stress distribution remained consistent for the experimentally determined elastic properties and the RVE-based material definitions indicates that the optimized candidate geometry was not merely tuned to a single constitutive input set but exhibited a robust stress homogenizing behavior across the investigated weight fractions.

Beyond the aluminum microparticle-reinforced epoxy adhesive system considered here, the same RVE-based framework could be extended to polymer matrices reinforced with carbon-based nanostructures, such as carbon nanotube–graphene hybrid systems and laser-structured carbon networks [32,33]. Such an extension would allow the effects of nanoscale morphology and conductive-network formation on the effective material response to be examined in future simulations.

5. Conclusions

This study presents a comprehensive method for developing an optimized cruciform specimen to more reliably characterize the in-plane biaxial mechanical behavior of particle-reinforced epoxy adhesives. This method integrates material-level validation steps with the geometry-level optimization process. In the first stage, the elastic modulus obtained from uniaxial tensile tests was verified using the RVE-based micromechanical analyses for each of 2, 6, and 10 wt%, where the mean modulus exhibited only small relative deviations (approximately +0.8–0.9% for 2 wt%, −1.0 to −2.1% for 6 wt%, and +1.1–1.9% for 10 wt%). This very low difference confirms the accuracy and consistency of the material models used in the finite element analyses. In addition, the comparative evaluations performed using both the experimentally determined elastic properties and the selected RVE-predicted engineering constants for the 2, 6, and 10 wt% materials provided further support for the reliability of the adopted material descriptions in the cruciform specimen analyses.

The dynamic XGBoost-MaxLIPOTR algorithm, tailored explicitly for the shape optimization of the cruciform specimen, resulted in significant improvements in stress homogeneity in the measurement region. For the effective gauge zone considered, the optimized candidate geometry produced highly consistent improvements in stress homogeneity for the 2, 6, and 10 wt% materials under both material descriptions. When the experimentally

determined elastic properties were used, the uniformity improvement was about 54% for the equivalent stress S_{eqv}, about 26% for the normal stress components S_{11} and S_{22}, and about 30% for the shear stress component S_{12}. Nearly identical levels of improvement were also obtained when the selected RVE-predicted engineering constants were employed. This close agreement across the investigated weight fractions and material descriptions indicates that the stress homogenizing effect of the optimized candidate geometry is not dependent on a specific material property set, but rather arises from the improved load-transfer path established by the optimized fillet transitions and center thickness. Accordingly, a more stable and continuous stress transfer from the specimen arms to the gauge zone was achieved. Furthermore, the optimum values of the fillet radius R and center thickness t predicted by the surrogate model were in close agreement with those numerically verified by the FEA results, confirming the convergence accuracy and stability of the adaptive optimization procedure. Therefore, this adaptive optimization framework can produce more stable and highly accurate results.

Future work may extend the present numerical shape optimization framework toward broader validation conditions and expanded design spaces. DIC-based biaxial strain-field measurements may be used to directly evaluate gauge-zone strain homogeneity and failure localization in the optimized candidate geometry. Additional loading scenarios, including unequal biaxial loading ratios, off-axis loading conditions, and non-proportional loading paths, may also be considered to assess the geometry's robustness beyond the elastic, equal-biaxial loading condition investigated in this study. From a numerical design perspective, the reduced R–t design space may be expanded by incorporating additional geometric variables, such as arm width, local tapering, slit/slot configuration, gauge-zone shape, and local thickness transitions, to further evaluate stress homogeneity, load-transfer efficiency, and failure localization within broader parametric or topology-optimization frameworks.

Author Contributions: B.E.: conceptualization, software, analysis, visualization, and writing—original draft; M.K.A.: supervision, project administration, and writing—review and editing. All authors have read and agreed to the published version of the manuscript.

Funding: This research was funded by the Scientific Research Projects Coordination Unit (BAP) of Erciyes University, grant number FDK-2023-12558.

Data Availability Statement: The data presented in this study is available on request from the authors.

Acknowledgments: The article complies with national and international research and publication ethics. Ethics Committee approval was not required for this study. This study is a part of a doctoral thesis titled 'Investigation of Biaxial Mechanical Behavior of Microparticle Reinforced Composite Adhesives' by Burak Ergunes, a student in the Graduate School of Natural and Applied Sciences at Erciyes University. During the preparation of this manuscript, the authors used a grammar-checking tool solely for grammar checking, language refinement, readability, and clarity. The authors reviewed and edited the output and take full responsibility for the content of this publication.

Conflicts of Interest: The authors declare no conflicts of interest.

References

1. Dorduncu, M.; Apalak, M.K.; Reddy, J.N. Stress wave propagation in adhesively bonded functionally graded cylinders: An improved model. *J. Adhes. Sci. Technol.* **2019**, *33*, 156–186. [CrossRef]
2. Razavi, N.; Ayatollahi, M.R.; Nemati Giv, A.; Khoramishad, H. Single lap joints bonded with structural adhesives reinforced with a mixture of silica nanoparticles and multi walled carbon nanotubes. *Int. J. Adhes. Adhes.* **2018**, *80*, 76–86. [CrossRef]
3. Pereira, A.B.; Fernandes, F.A.O.; de Morais, A.B.; Maio, J. Biaxial Testing Machine: Development and Evaluation. *Machines* **2020**, *8*, 40. [CrossRef]

4. Ramault, C. Guidelines for Biaxial Testing of Fibre Reinforced Composites Using a Cruciform Specimen. Ph.D. Thesis, Vrije Universiteit Brussel, Brussels, Belgium, 2012.
5. Tiernan, P.; Hannon, A. Design optimisation of biaxial tensile test specimen using finite element analysis. *Int. J. Mater. Form.* **2014**, *7*, 117–123. [CrossRef]
6. Xu, C.; Song, L.; Zhu, H.; Meng, S.; Xie, W.; Jin, H. Experimental investigation on the mechanical behaviour of 3D carbon/carbon composites under biaxial compression. *Compos. Struct.* **2018**, *188*, 7–14. [CrossRef]
7. Deland, D.; Zhang, Z.; Kirane, K. Biaxial flexural failure of woven composite plates investigated by the ring on ring bending test. *Thin-Walled Struct.* **2020**, *148*, 106585. [CrossRef]
8. Makris, A.; Vandenbergh, T.; Ramault, C.; Van Hemelrijck, D.; Lamkanfi, E.; Van Paepegem, W. Shape optimisation of a biaxially loaded cruciform specimen. *Polym. Test.* **2010**, *29*, 216–223. [CrossRef]
9. Horta Muñoz, S.; Serna Moreno, M.d.C. Advances in cruciform biaxial testing of fibre-reinforced polymers. *Polymers* **2022**, *14*, 686. [CrossRef]
10. Smits, A.; Van Hemelrijck, D.; Philippidis, T.P.; Cardon, A. Design of a cruciform specimen for biaxial testing of fibre reinforced composite laminates. *Compos. Sci. Technol.* **2006**, *66*, 964–975. [CrossRef]
11. Schemmann, M.; Lang, J.; Daniel, M.; Kehrer, L.; Weidenmann, K.A.; Schmauder, S. Cruciform Specimen Design for Biaxial Tensile Testing of Sheet Molding Compound (SMC). *J. Compos. Sci.* **2018**, *2*, 12. [CrossRef]
12. Upadhyay, M.V.; Panzner, T.; Van Petegem, S.; Van Swygenhoven, H. Stresses and Strains in Cruciform Samples Deformed in Tension. *Exp. Mech.* **2017**, *57*, 905–920. [CrossRef]
13. Zhang, X.; Zhu, H.; Lv, Z.; Zhao, X.; Wang, J.; Wang, Q. Investigation of biaxial properties of CFRP with the novel-designed cruciform specimens. *Materials* **2022**, *15*, 7034. [CrossRef]
14. Chen, J.; Zhang, J.; Zhao, H. Designing a cruciform specimen via topology and shape optimisations under equal biaxial tension using elastic simulations. *Materials* **2022**, *15*, 5001. [CrossRef]
15. Gower, M.R.L.; Shaw, R.M. Towards a planar cruciform specimen for biaxial characterisation of polymer matrix composites. *Appl. Mech. Mater.* **2010**, *24–25*, 115–120. [CrossRef]
16. Gutiérrez, J.C.; Lozano, A.; Manzano, A.; Flores, M.S. Numerical and experimental analysis for shape improvement of a cruciform composite laminates specimen. *Fibres Text. East. Eur.* **2016**, *24*, 89–94. [CrossRef]
17. Youssef, Y.; Labonté, S.; Roy, C.; Lefebvre, D. Specimen design, manufacturing and testing procedures for flat carbon fiber reinforced plastic laminates under biaxial loading. *Polym. Compos.* **1998**, *19*, 257–263. [CrossRef]
18. Lamkanfi, E.; Van Paepegem, W.; Degrieck, J. Shape optimization of a cruciform geometry for biaxial testing of polymers. *Polym. Test.* **2015**, *41*, 7–16. [CrossRef]
19. Mulay, A.; Bagul, V. Design optimization of the cruciform specimen in a biaxial test using MADM methods. *Aust. J. Mech. Eng.* **2022**, *20*, 792–802. [CrossRef]
20. Yang, X.; Wu, Z.R.; Yang, Y.R.; Pan, Y.; Wang, S.Q.; Lei, H. Optimization design of cruciform specimens for biaxial testing based on genetic algorithm. *J. Mater. Eng. Perform.* **2023**, *32*, 2330–2343. [CrossRef]
21. Zhang, Z.Q.; Li, P.J.; Li, Q.K.; Dong, X.; Lu, X.G.; Zhang, Y.F. Dynamic machine learning global optimization algorithm and its application to aerodynamics. *J. Propuls. Power* **2023**, *39*, 524–539. [CrossRef]
22. *ASTM D638-22*; Standard Test Method for Tensile Properties of Plastics. ASTM International: West Conshohocken, PA, USA, 2022.
23. Ege Nanotek. Alüminyum Tozu—Al | Mikronize Alüminyum Tozu—Al Mikro Tozu. Available online: https://www.egenanotek.com/kategori/mikronize-aluminyum-tozu-al-mikro-tozu (accessed on 27 December 2025).
24. Farkash, A.; Mittelman, B.; Hayun, S.; Priel, E. Aluminum Matrix Composites with Weak Particle Matrix Interfaces: Effective Elastic Properties Investigated Using Micromechanical Modeling. *Materials* **2021**, *14*, 6083. [CrossRef] [PubMed]
25. Kisling AG. 7440 Epoxy Structural Adhesive. Available online: https://www.kisling.com/en/products/product-overview/7440-epoxy-structural-adhesive (accessed on 27 December 2025).
26. ANSYS. Material Designer User's Guide. Available online: https://ansyshelp.ansys.com/public/Views/Secured/corp/v251/en/pdf/Material_Designer_Users_Guide.pdf (accessed on 27 December 2025).
27. Richardson, L.F. The approximate arithmetical solution by finite differences of physical problems involving differential equations, with an application to the stresses in a masonry dam. *J. Philos. Trans. R. Soc. Lond. Ser. A* **1911**, *210*, 307–357. [CrossRef]
28. Roache, P.J. Quantification of uncertainty in computational fluid dynamics. *Annu. Rev. Fluid Mech.* **1997**, *29*, 123–160. [CrossRef]
29. Celik, I.B.; Ghia, U.; Roache, P.; Freitas, C.J. Procedure for estimation and reporting of uncertainty due to discretization in CFD applications. *J. Fluids Eng. Trans. ASME* **2008**, *130*, 078001.
30. Dexl, F.; Hauffe, A.; Markmiller, J.; Wolf, K. Numerical optimization-based design studies on biaxial tensile tests. *Proc. Inst. Mech. Eng. Part C J. Mech. Eng. Sci.* **2023**, *237*, 4358–4379. [CrossRef]
31. Lu, Z.; Zhao, J.-Y.; Zhou, C.-Y.; He, X.-H. Optimization design of a small-sized cruciform specimen for biaxial fatigue testing. *Metals* **2020**, *10*, 1148. [CrossRef]

32. Kuksin, A.V.; Morozova, A.S.; Vasilevskaya, Y.O.; Eganova, E.M.; Popovich, K.D.; Gerasimenko, A.Y. Dry electrodes based on carbon nanotubes–graphene hybrid nanostructures for long-term ECG monitoring. *Diam. Relat. Mater.* **2025**, *159*, 112895. [CrossRef]
33. Morozova, A.S.; Kuznetsova, E.A.; Guslyantsev, E.E. Formation mechanisms of flexible strain-sensitive sensors based on carbon nanostructures with laser formation for a post-traumatic joint rehabilitation monitoring system. *Biomed. Eng.* **2026**. [CrossRef]

Disclaimer/Publisher's Note: The statements, opinions and data contained in all publications are solely those of the individual author(s) and contributor(s) and not of MDPI and/or the editor(s). MDPI and/or the editor(s) disclaim responsibility for any injury to people or property resulting from any ideas, methods, instructions or products referred to in the content.